



How is particulate organic carbon transported through the river-fed submarine Congo Canyon to the deep sea?

Sophie Hage¹, Megan L. Baker², Nathalie Babonneau¹, Guillaume Soulet¹, Bernard Dennielou¹, Ricardo Silva Jacinto¹, Robert G. Hilton³, Valier Galy⁴, François Baudin⁵, Christophe Rabouille⁶, Clément Vic⁷, Sefa Sahin⁸, Sanem Açıkalın⁸, and Peter J. Talling²

¹Geo-Ocean, UMR6538, Univ Brest, Ifremer, CNRS, Plouzané, France

²Departments of Geography and Earth Sciences, Durham University, Durham, UK

³Department of Earth Sciences, University of Oxford, Oxford, UK

⁴Department of Marine Chemistry and Geochemistry, Woods Hole Oceanographic Institution, Woods Hole, MA 02543, USA

⁵ISTeP, UMR 7193, Sorbonne Université, CNRS, Paris, France

⁶LSCE, UMR 8212, CEA-CNRS-UVSQ, IPSL and Université Paris-Saclay, Gif-sur-Yvette, France

⁷Univ Brest, CNRS, Ifremer, IRD, Laboratoire d’Océanographie Physique et Spatiale (LOPS), IUEM, Plouzané, France

⁸School of Natural and Environmental Sciences, Newcastle University, Newcastle, UK

Correspondence: Sophie Hage (sophie.hage@hotmail.com)

Received: 30 March 2024 – Discussion started: 4 April 2024

Revised: 19 July 2024 – Accepted: 16 August 2024 – Published: 30 September 2024

Abstract. The transfer of carbon from land to the near-coastal ocean is increasingly being recognized in global carbon budgets. However, a more direct transfer of terrestrial organic carbon to the deep sea is comparatively overlooked. Among systems that connect coastal to deep-sea environments, the submarine Congo Canyon is of particular interest since the canyon head starts 30 km into the Congo River estuary, which delivers $\sim 7\%$ of the dissolved and particulate organic carbon from the world’s rivers. However, sediment and particulate organic carbon transport mechanisms that operate in the Congo Canyon and submarine canyons more globally are poorly constrained compared to rivers because monitoring of deep-sea canyons remains challenging. Using a novel array of acoustic instruments, sediment traps, and cores, this study seeks to understand the hydrodynamic processes that control delivery of particulate organic carbon via the submarine Congo Canyon to the deep sea. We show that particulate organic carbon transport in the canyon axis is modulated by two processes. First, we observe periods where the canyon dynamics are dominated by tides, which induce a background oscillatory flow (speeds of up to 0.15 m s^{-1}) through the water column, keeping muds in suspension, with a net upslope transport direction. Second, fast-moving (up to 8 m s^{-1}) turbidity currents occur for 35 % of the time dur-

ing monitoring periods and transport particulate organic carbon with mud and sand at an estimated transit flux that is more than 3 to 6 times the flux induced by tides. Organic carbon transported and deposited in the submarine canyon has a similar isotopic composition to organic carbon in the Congo River and in the deep-sea fan at 5 km of water depth. Episodic turbidity currents thus promote efficient transfer of river-derived particulate organic carbon in the Congo submarine fan, leading to some of the highest terrestrial carbon preservation rates observed in marine sediments globally.

1 Introduction

Earth’s carbon is exchanged between land, ocean, and atmosphere reservoirs, regulating life and climate over daily to geological timescales. The land and ocean carbon reservoirs are usually quantified separately in global carbon cycle models and viewed in terms of their carbon exchanges with the atmosphere (Ciais et al., 2013; Friedlingstein et al., 2023). However, an emerging view of the global carbon cycle is now taking into account the role of land to ocean transport of carbon, which is a potential source or sink of atmospheric CO_2 (Galy et al., 2015; Regnier et al., 2013, 2021). It has long

been thought that most (90 %) terrestrial sediment and particulate carbon reaching the ocean stays on deltas and continental shelves (Bernier, 1982; Burdige, 2007; Tegler et al., 2024), particularly during sea level highstands (Posamentier and Kolla, 2003). However, an increasing number of studies have revealed that large volumes of terrestrial and shelf sediment can be transferred via submarine canyons to the deep sea, where it is buried in depositional systems called deep-sea fans (e.g., Canals et al., 2006; Galy et al., 2007; Kao et al., 2014; Rabouille et al., 2019; Talling et al., 2024). Submarine canyons are ubiquitous on the ocean floor, where more than 5000 canyons have been mapped (Harris and White-way, 2011). Despite their global occurrence and importance for carbon cycling, submarine canyons remain poorly investigated compared to river systems on land. This is because particulate transport in submarine canyons includes seafloor sediment flows called turbidity currents, which are episodic, challenging to measure, and can damage monitoring instruments (Khrifounoff et al., 2003; Sumner and Paull, 2014; Hughes Clarke, 2016; Talling et al., 2023). Transport processes in submarine canyons are thus poorly constrained, with understanding still mostly based on interpretation of seabed sediments and modeling (Bouma, 1962; Symons et al., 2017; Cartigny et al., 2014; Miramontes et al., 2020; Ge et al., 2022).

A major step forward in understanding sediment transfer in submarine canyons was made possible in the past 2 decades through advances in technology that enabled direct measurements of sediment transport processes in canyons (Puig et al., 2014; Talling et al., 2023). Observations show that turbidity currents are the main transport process for moving material down canyon (e.g., Congo, Monterey, Whittard, Var, and Capbreton canyons; Khrifounoff et al., 2003, 2012; Azpiroz-Zabala et al., 2017; Paull et al., 2018; Maier et al., 2019; Simmons et al., 2020; Guiastrennec-Faugas et al., 2020; Talling et al., 2022). These flows last from a few minutes to up to a few days and sometimes travel at high speed (e.g., 19 m s^{-1} ; Heezen and Ewing, 1952). However, other more continuous processes such as tidally induced currents (external and internal tides) or dense shelf water cascading can also occur in submarine canyons (Canals et al., 2006; Puig et al., 2014). Oscillating tidal currents, with directions that reverse up canyon to down canyon, typically have speeds of up to 0.3 m s^{-1} . But in a few locations, oscillations due to tides and winds can sometimes reach moderate velocities (up to 1 m s^{-1} ; e.g., Monterey, Capbreton, Logan, Whittard and Cassidaigne canyons; Mulder et al., 2012; Maier et al., 2019; Li et al., 2019; Heijnen et al., 2022; Brun et al., 2023). Yet, the way background oscillatory flows and episodic turbidity currents interact and combine to transport sediment and particulate organic carbon to the deep sea is poorly constrained. This lack of understanding inhibits an accurate assessment of sediment and carbon transport from continental shelves to the deep sea.

In this study, we use direct observations of transport processes and sampling of particulate organic carbon from the submarine Congo Canyon water column and seabed. The submarine Congo Canyon provides a unique opportunity to test how particulate organic carbon transport by rivers on land continues into the ocean because the canyon head starts within the Congo River estuary (Fig. 1). This connection is important because the Congo River ranks fifth in terms of global particulate organic carbon export to the ocean (Coynel et al., 2005). The submarine Congo Canyon continues as a less deeply incised submarine channel, beyond which is an area termed a lobe, where flows become unconfined and very rapid sedimentation occurs (Babonneau et al., 2002; Dennielou et al., 2017). The lobe is at 5 km water depth and constitutes a sink of organic carbon, with estimated burial rates of 0.42 MtCyr^{-1} , equalling 19 % of the total organic carbon buried annually in the southern Atlantic Ocean at $> 3000 \text{ m}$ water depth (Rabouille et al., 2019; Mollenhauer et al., 2004). The submarine canyon, channel, and lobe together form the Congo submarine fan. The Congo submarine fan has received widespread attention in the past 2 decades (e.g., Savoye et al., 2000; Babonneau et al., 2002, 2010; Khrifounoff et al., 2003; Rabouille et al., 2009, 2017a, b, 2019; Baudin et al., 2010, 2017, 2020; Stetten et al., 2015; Dennielou et al., 2017; Talling et al., 2022; Pope et al., 2022). A range of hydrodynamic processes has been directly observed (Khrifounoff et al., 2003; Azpiroz-Zabala et al., 2017; Talling et al., 2022). For example, both occasional and fast (up to 3.5 m s^{-1}) turbidity currents and continuous internal tides featuring rather slow currents (up to 10 cm s^{-1}) were detected in 2004 in the distal channel, which is 1000 km downstream of the river estuary (Vangriesheim et al., 2009). Measurements in 2010 and 2013 showed that turbidity currents in the proximal canyon last for up to a week, occur for 35 % of the time during monitoring periods, and reach speeds of $2\text{--}3 \text{ m s}^{-1}$ (Azpiroz-Zabala et al., 2017; Simmons et al., 2020). More recently, 14 turbidity currents were detected in the upper Congo Canyon, including one flow that traveled $> 1130 \text{ km}$ while accelerating from 5.2 to 8.0 m s^{-1} , breaking seabed communication cables and moorings on 14–16 January 2020 (Talling et al., 2022). Despite numerous studies of the Congo submarine fan, important questions remain related to hydrodynamic processes and associated carbon transfer in the canyon towards the deep sea.

This paper aims to further our understanding of carbon transport in the submarine Congo Canyon by linking particulate organic carbon measurements with direct observations and sampling of flows in the canyon obtained in 2019–2020 for the first time. The following three questions will be discussed. First, what are the hydrodynamic processes controlling the transport of particulate organic carbon in the submarine Congo Canyon? In particular, what is the relative importance of tidally induced currents compared to faster but more episodic turbidity currents. Second, how does the composition and age of organic carbon transiting through the canyon

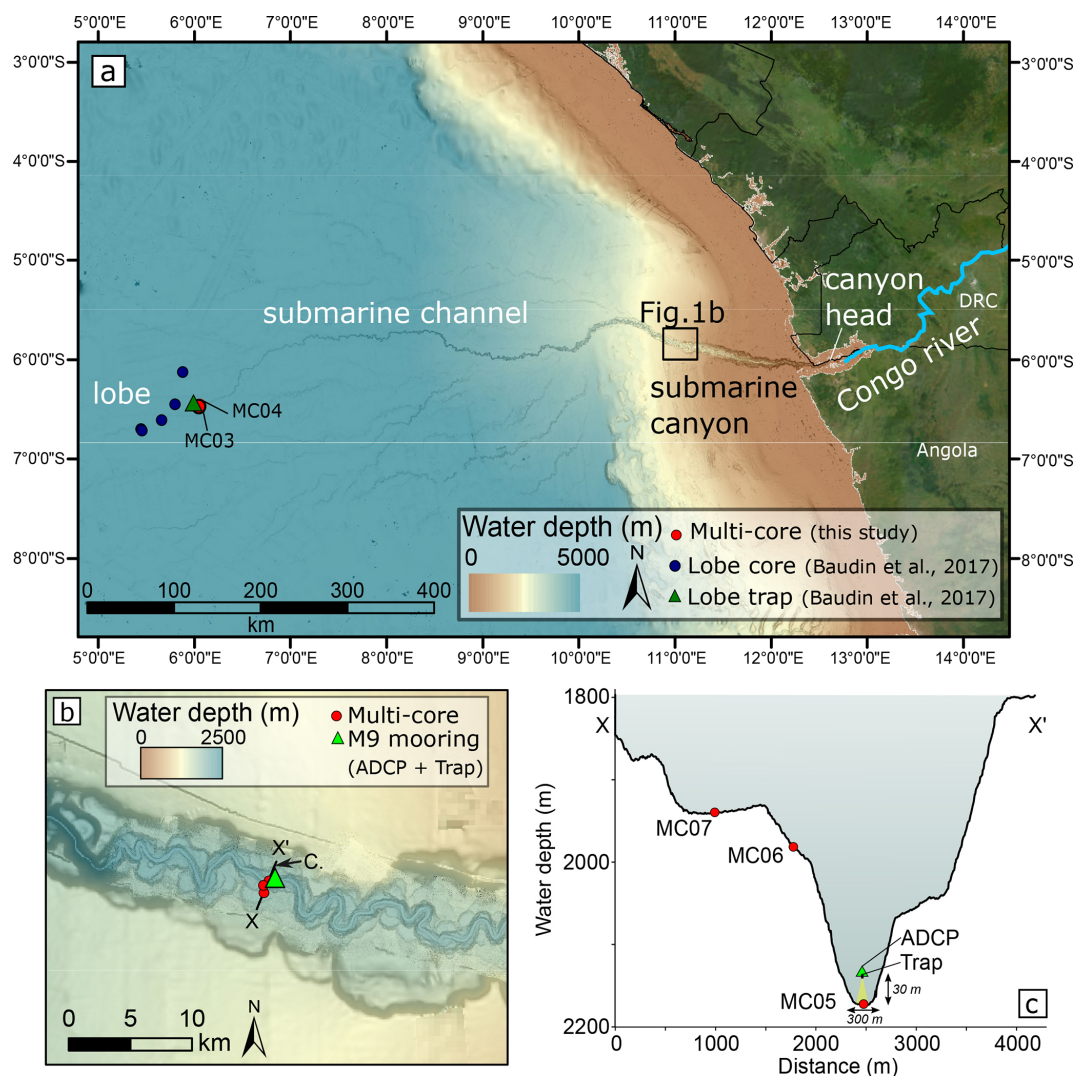


Figure 1. The Congo River and submarine system. (a) Map of the Congo River and bathymetry of its connected submarine canyon and channel terminating onto distal lobe. Locations of distal channel multi-cores collected for this study during James Cook cruise 187 (JC187) and the piston cores and sediment trap deployed 45 m above the seabed in the lobe area are shown (Baudin et al., 2017). DRC denotes the Democratic Republic of Congo. (b) Location of the moored instruments (M9 mooring in Talling et al., 2022) and the multi-cores used in this study in the submarine Congo Canyon at 2190 m water depth. (c) Cross-section across the submarine canyon showing the locations of the acoustic Doppler current profiler (ADCP), sediment trap, and multi-cores.

and deposited on the deep-sea lobe compare to that of particulate organic carbon in the Congo River? This comparison allows us to discuss the efficiency of terrestrial organic carbon transport to the deep-sea carbon reservoir. Third, how do hydrodynamic processes and associated carbon transport in the submarine Congo Canyon compare with submarine canyons in different settings? This leads us to briefly discuss the implications for the redistribution of carbon between two globally important carbon reservoirs (i.e., terrestrial biosphere and ocean sediments).

2 The Congo River and deep-sea fan system

2.1 The Congo River and connected submarine canyon

The Congo River is the second largest river in the world in terms of drainage area ($3.7 \times 10^6 \text{ km}^2$). The hydrological regime of the lower river (Brazzaville–Kinshasa gauging station) is equatorial with limited annual fluctuations and an average annual discharge of $40\,500 \text{ m}^3 \text{ s}^{-1}$ for the years 1903–2020 (Laraque et al., 2022). The Congo River mouth forms an estuary under a microtidal regime (up to 1.9 m tidal range; Vallaeys et al., 2021). A submarine canyon starts 30 km into the river estuary from the coast. This canyon is 300 km long,

10 km wide, up to 800 m deep, and characterized by multiple terrace levels (Fig. 1a; Heezen et al., 1964). The canyon then evolves into a 600 km long channel overhung by levees and terminates to distal depositional lobes at 5 km of water depth (Savoye et al., 2000; Babonneau et al., 2002). Downslope turbidity currents were directly observed in the channel (Khripounoff et al., 2003; Vangriesheim et al., 2009) and more recently in the canyon (Azpiroz-Zabala et al., 2017; Simmons et al., 2020; Talling et al., 2022) using moored current meters (Fig. 2). A total of 14 turbidity currents were measured over 4 months in 2019 and 2020 in the proximal canyon at a site 200 km downstream of the Congo River mouth (Talling et al., 2022). One of these flows traveled more than 1100 km down the canyon and channel system, reaching transit velocities of 8 m s^{-1} and damaging instrumented moorings and seabed telecommunication cables. An estuarine interplay of river floods combined with spring tides is suggested as the triggering mechanism for those flows (Talling et al., 2022); however, more direct observations are needed to test this hypothesis.

2.2 Past studies of particulate organic carbon in the Congo River and deep-sea fan system

The Congo River exports ca. 2 Mt C yr^{-1} of particulate organic carbon annually, ranking fifth in terms of particulate organic carbon export by rivers globally (Coynel et al., 2005). The composition of this riverine carbon is dominated by C3 plant debris derived from the rainforest vegetation and by pre-aged soil from the Cuvette Congolaise swamp forest (Spencer et al., 2012; Hemingway et al., 2017), with additional minor contributions from freshwater phytoplankton and C4 plant-derived organic matter. The contribution of fresh C3 vegetation was shown to increase with elevated river discharge (Hemingway et al., 2017). River-suspended sediment samples measured for organic carbon composition show wide ranges of total organic carbon contents (TOC from 5.7 % to 11.8 %), carbon stable isotope ($\delta^{13}\text{C}$ from -28.8‰ to -24.6‰), and radiocarbon isotope compositions ($\delta^{14}\text{C}$ from -309‰ in the fine particulate organic carbon fraction to 95.7‰ in the coarse particulate organic carbon fraction; Spencer et al., 2012; Hemingway et al., 2017).

Between 33 % and 69 % of the Congo River particulate organic carbon export is estimated to be deposited in the Congo submarine fan, including the canyon, channel, levees, and distal lobe environments based on geochemical measurements from surficial (20 cm deep) sediment (Rabouille et al., 2019; Stetten et al., 2015; Baudin et al., 2010, 2020). Longer piston sediment cores (up to 10 m long) from the channel and levees at 4 km water depth reveal that 70 % to 80 % of the organic matter is terrestrial and derived from the river (Baudin et al., 2010). Piston sediment cores were retrieved in 2019 from the canyon, covering a variety of grain sizes, with TOC contents ranging from 0.15 % to 11.3 % and $\delta^{13}\text{C}$ values from -28.5‰ to -26.2‰ that are similar to samples

from the Congo River (Baker et al., 2024). The only marine signature for organic carbon composition in the Congo submarine fan was found in a sediment trap located 45 m above the seabed at 4779 m water depth in the distal channel-lobe transition zone (Fig. 1a, Baudin et al., 2017). TOC contents in this sediment trap vary between 3.9 % and 5.6 %, whereas $\delta^{13}\text{C}$ ranges from -24.4‰ to -22.7‰ (Baudin et al., 2017).

3 Methods

3.1 Oceanographic observations

In this study we focus on data recovered from one mooring (M9 in Talling et al., 2022, Fig. 1) that included one downward-looking 600 kHz acoustic Doppler current profiler (ADCP) and a sediment trap located 32 m above the seabed. Our studied mooring (M9) is located 200 km off the river mouth at 2190 m water depth in the canyon thalweg. At this location, the canyon thalweg is incised by 500 m and has two terrace levels 200 and 250 m above the thalweg. The ADCP instrument recorded velocity data in three directions (eastward, northward, and vertical) at 11 s intervals, with a vertical cell size of 0.75 m. All three velocity directions were combined to generate a velocity magnitude (V_{mag}) matrix. Elevated values of V_{mag} allow turbidity current events to be identified. In total, 14 turbidity currents were detected in the Congo Canyon between 15 September 2019 and 14 January 2020. In this study, we focus on the first 8 turbidity currents (between 15 September and 10 December 2019) out of the 14 events detected in the full time series recorded at mooring M9. The last 6 flows are not further considered here because they were not identified in the sediment trap due to disturbance in the trap top (Fig. S1 in the Supplement).

To further analyze the motion of water and particles in the canyon between turbidity current events, the ADCP's eastward and northward velocities were turned into V_{along} (velocity along canyon) and V_{cross} (velocity across canyon) using the direction of the canyon axis at our mooring location. Hodographs were created for two V_{along} arrays 5 and 30 m above canyon floor. Hodographs are progressive vector diagrams showing how velocity vectors change with time from a fixed, common origin, with our M9 mooring location chosen as the origin. Finally, a frequency analysis was carried out on the ADCP velocity data to identify the main period peaks in velocity oscillations to be correlated with known hydrodynamic processes such as tides. Power spectral densities were computed using the Welch method from the data binned on a regular 10 min grid, with 2048 bin segments and a half-segment overlap (Welch, 1967).

We also present data from one conductivity–temperature–depth profiler (CTD) cast, which was collected at the M9 location on 19 September 2019, when there was no turbidity current event. The instrument is a WetLab Eco BBRTS scattering meter, which provided salinity (in PSU), oxygen

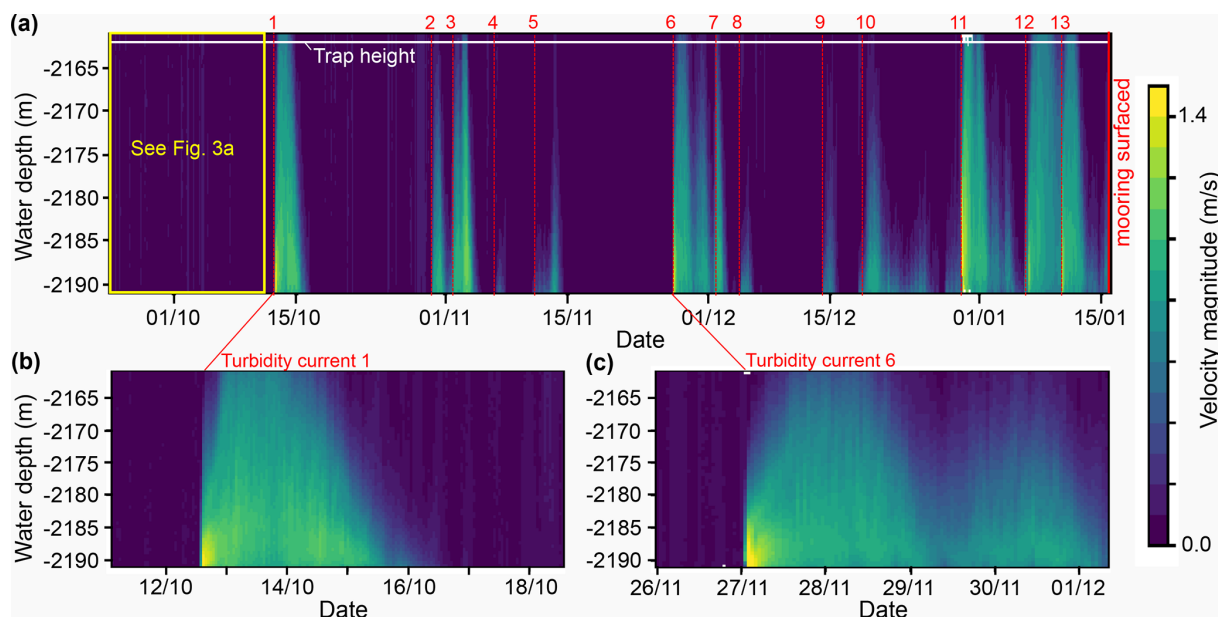


Figure 2. Velocity magnitude measured by a 600 kHz acoustic Doppler current profiler deployed 32 m above the seabed in the submarine Congo Canyon (see Fig. 1b for location). (a) Time series between 21 September 2019 and 15 January 2020. Numbers in red denote turbidity current events. (b) A zoomed-in view of turbidity current event 1. (c) A zoomed-in view of turbidity current event 6, which is made of two pulses.

(in $\mu\text{mol kg}^{-1}$), temperature (in $^{\circ}\text{C}$), and turbidity (in m^{-1}) profiles from water surface to canyon floor at 2190 m water depth.

3.2 Sediment trap and seabed sampling

An Anderson-type sediment trap (Anderson, 1977) was deployed on the same mooring line as our studied ADCP to collect particles transported in the canyon. Anderson traps are made of an open top funnel of 25 cm in diameter above a 110 cm long plastic liner tube (6 cm in diameter) allowing fallen sedimentary sequences to be preserved in a similar way to seabed sediment cores (e.g. Liu et al., 2016; Maier et al., 2019). An intervalometer unit was included in the funnel to insert disks that were scheduled to fall every 21 d into the liner tube. The timing of trapped particles could then be precisely compared with the timing of turbidity current events detected by the ADCP. Once retrieved from the sea, the trap was X-rayed and scanned for sediment properties using a Geotek X-ray CT Core Imaging System (MSCL-XCT). Then, 78 total 1 cm thick samples were extruded from the trap liner. The top 25 cm of sediment in the trap was disturbed and thus not included in our sample set (Fig. S1).

Multi-cores (50 cm deep maximum) were collected in the canyon thalweg and on two terrace levels (at 1932 and 2007 m water depth) near the M9 mooring location in the canyon axis. Two multi-coring sites were also studied in the distal channel at 4795 and 4765 m water depth, located in the channel thalweg and levee, respectively. These sites were

used to compare the seabed carbon composition found in the upper canyon at M9 at a water depth of 2190 m and 800 km downstream of the M9 location along the canyon channel axis. In total, 13 samples from multi-cores were analyzed, including three samples (45, 25, and 5 cm deep) per multi-coring site in the canyon thalweg and two terrace levels and two samples (45 and 5 cm) per multi-coring site in the distal channel thalweg and levee.

All 91 samples collected from the trap and the six multi-cores were analyzed for grain size using Beckman Coulter LS 13 320 laser diffraction particle size analyzer at the Department of Geography, Durham University. A total of 20 mL of 20 % hydrogen peroxide was added to ~ 0.5 g of sediment sample to remove organics before the sample was centrifuged to remove the supernatant. Samples were then mixed with 20 mL of deionized water and 2 mL of sodium hexametaphosphate solution to limit flocculation. Samples were run through the analyzer three times; the runs were compared, and if they were similar then the results were averaged. The D50 (i.e., median grain size) and D90 (i.e., the particle diameter where 90 % of the distribution has a smaller particle size) were computed and are presented in this study. All samples were then measured for organic carbon geochemistry as described below.

3.3 Organic carbon geochemistry

3.3.1 Sample preparation and total organic carbon content

Samples were freeze-dried, ground into powder, and rinsed with deionized water to remove salt prior to all organic carbon geochemistry measurements. To determine the total organic carbon content (TOC) of samples, between 4 and 6 mg of sample was weighed into silver capsules. Between 100 and 200 μL of 1 M hydrochloric acid was added to each capsule to remove inorganic carbon (i.e., carbonates). Capsules were then inserted into a LECO elemental analyzer to measure TOC and total nitrogen (TN) contents in duplicates at the Panoply platform (Paris-Saclay, France). Triplicate TOC measurement was conducted for each sample at the FOCUS Isotopy platform (ULiège, Belgium). The mean value between replicates is given (Table 1), and the uncertainty is taken as the standard deviation between replicates. The average standard deviation between is 0.02 % for TN duplicates ($n = 182$) and 0.30 % for TOC triplicates ($n = 273$).

3.3.2 Organic carbon stable isotopes

Organic carbon stable isotopes (reported as $\delta^{13}\text{C}$ values) were measured to determine the terrestrial or marine origin of the samples (Hecky and Hesslein, 1995). Knowing the TOC of each sample, we weighed adequate masses (between 1 and 3 mg) into silver capsules for optimal measurement of the organic carbon stable isotope by mass spectrometry. Samples were acidified with 1 M hydrochloric acid to remove inorganic carbon. They then were measured for $\delta^{13}\text{C}$ in triplicate by isotope ratio mass spectrometry (IRMS) using a Thermo Fisher Scientific DELTAplus XP coupled to a Flash Elemental Analyzer 1112 Series at the Panoply Platform (Paris-Saclay, France) and an Elementar precISION coupled to a VarioMicro Elementar at the FOCUS Research Unit (ULiège, Belgium). Results are reported in per mill relative to the Vienna PeeDee Belemnite (VPDB) standard. Presented values correspond to the mean value between triplicates, and uncertainty is taken as the standard deviation of triplicates. The average standard deviation between $\delta^{13}\text{C}$ triplicates ($n = 273$) is 0.37 ‰.

3.3.3 Radiocarbon

Radiocarbon (^{14}C) was measured on 30 samples (out of the 91, see Table 2) to determine the ^{14}C composition of the organic carbon transported and deposited in the submarine canyon and channel. The ^{14}C composition of organic matter relates to its age (recent, pre-aged, or geologic) and is a crucial information regarding its reactivity, and thus its tendency to be mineralized if labile or be sequestered from the atmosphere for long timescales if refractory (Hemingway et al., 2019). Radiocarbon measurements were carried out at the UK National Environmental Isotope Facil-

ity (NEIF). Sediment samples were acidified by fumigation with concentrated (37.3 %) hydrochloric acid to remove any trace of inorganic carbon. Organic carbon was then converted to CO_2 through combustion and purified cryogenically following NEIF standard procedures (Ascough et al., 2024). An aliquot of the purified CO_2 was used to determine its $\delta^{13}\text{C}$ (‰ VPDB) by IRMS (Thermo Fisher Delta V). A further aliquot was graphitized following NEIF procedures (Ascough et al., 2024) to measure its ^{14}C composition by accelerator mass spectrometry (AMS). Radiocarbon measurements were corrected for isotopic fractionation using the measured $\delta^{13}\text{C}$ value by IRMS. Radiocarbon results were reported in the form of the fraction modern ($F^{14}\text{C}$) (Reimer et al., 2004), identical to the $A_{\text{SN}}/A_{\text{ON}}$ (Stuiver and Polach, 1977) and $^{14}\text{a}_\text{N}$ (Mook and van der Plicht, 1999) metrics. Comparing the ^{14}C composition of samples of different calendar ages is challenging because of changing atmospheric ^{14}C composition with time, especially for post-Atomic Age (> 1950) samples and ^{14}C decay (Soulet et al., 2016; Skinner and Bard, 2022). A way to make comparable radiocarbon data obtained from samples formed at different calendar years is to normalize them to the radiocarbon composition of the atmosphere when the samples formed. This metric is called the isotopic relative enrichment $F^{14}\text{R}$ (Soulet et al., 2016). Hence, our radiocarbon data are reported as the $F^{14}\text{R}$ metric relative to the ^{14}C composition of the atmosphere of year 2019 (i.e., when the samples were collected): $F^{14}\text{R} = F^{14}\text{C}_{\text{sample}}/F^{14}\text{C}_{\text{atm in 2019}}$. Radiocarbon data of samples from the literature (Spencer et al., 2012; Hemingway et al., 2017) were similarly reported relative to the $F^{14}\text{C}$ of the atmosphere in their collection year. The post-Atomic Age atmospheric ^{14}C reference dataset is taken from Hua et al. (2022).

3.3.4 Rock-Eval analyses

To further characterize the types of organic carbon and compare the carbon composition of our samples with samples from the Congo distal lobes (Baudin et al., 2017), all samples were analyzed by pyrolysis and oxidation using the Rock-Eval 6 Turbo device at the Paris Earth Science Institute (IS-TeP; Baudin et al., 2015). The desalted samples were heated in two successive stages. The first stage corresponds to the pyrolysis under an inert atmosphere (N_2), where the sample is heated at 180 °C for 3 min and then up to 650 °C at a ramp of 30 °C min^{-1} . The second stage is an oxidation of the residual carbon that has resisted pyrolysis under the laboratory atmosphere from 300 to 850 °C at a temperature ramp of 20 °C min^{-1} . During the pyrolysis phase, hydrocarbon (HC) effluents were monitored by a flame ionization detector, while CO and CO_2 were monitored by infrared detectors. During the oxidation phase, CO and CO_2 were monitored by infrared detectors. Hydrocarbon detected during the pyrolysis stage are expressed in milligrams of HC per gram of sample, whereas CO_2 evolved during the pyrolysis stage

Table 1. Grain size and organic carbon geochemistry measurement made on all samples collected in this study.

Sample number	Sample code	Sample type	D_{50} (μm)	D_{90} (μm)	TN (%)		TOC (%)		$\delta^{13}\text{C}$ (‰)		HI ($\text{mg CO}_2 \text{ g C}_{\text{Org}}^{-1}$)	OI ($\text{mg HC g C}_{\text{Org}}^{-1}$)
					mean	SD	mean	SD	mean	SD		
1	JC187-ST-22-23	Trap	6	22	0.30	0.03	4.4	0.4	-26.9	0.4	168	314
2	JC187-ST-23-24	Trap	6	23	0.29	0.00	4.5	0.5	-26.9	0.5	158	233
3	JC187-ST-24-25	Trap	7	29	0.30	0.02	4.3	0.3	-26.9	0.4	161	221
4	JC187-ST-25-26	Trap	7	27	0.29	0.01	4.5	0.2	-26.9	0.4	157	221
5	JC187-ST-26-27	Trap	6	26	0.29	0.00	4.5	0.3	-26.9	0.4	157	214
6	JC187-ST-27-28	Trap	9	40	0.29	0.00	4.3	0.3	-26.9	0.3	164	205
7	JC187-ST-28-29	Trap	8	38	0.29	0.02	4.4	0.3	-26.8	0.4	163	232
8	JC187-ST-29-30	Trap	12	53	0.27	0.01	4.1	0.3	-26.8	0.3	172	194
9	JC187-ST-30-31	Trap	18	56	0.23	0.01	3.4	0.3	-26.7	0.4	164	209
10	JC187-ST-31-32	Trap	15	57	0.29	0.03	4.2	0.2	-26.9	0.3	141	202
11	JC187-ST-32-33	Trap	5	22	0.27	0.01	4.1	0.4	-26.8	0.4	157	242
12	JC187-ST-33-34	Trap	5	24	0.26	0.00	4.0	0.3	-27.0	0.3	150	242
13	JC187-ST-34-35	Trap	11	47	0.24	0.02	3.9	0.3	-26.9	0.4	166	216
14	JC187-ST-35-36	Trap	9	47	0.27	0.01	4.2	0.2	-26.9	0.3	163	217
15	JC187-ST-36-37	Trap	7	33	0.27	0.04	4.3	0.7	-26.9	0.3	166	214
16	JC187-ST-37-38	Trap	7	39	0.25	0.00	4.2	0.3	-26.8	0.4	157	254
17	JC187-ST-38-39	Trap	22	51	0.17	0.00	2.7	0.3	-26.7	0.5	153	247
18	JC187-ST-39-40	Trap	34	74	0.14	0.01	2.4	0.2	-26.5	0.7	157	212
19	JC187-ST-40-41	Trap	31	71	0.13	0.00	2.2	0.2	-26.7	0.4	158	204
20	JC187-ST-41-42	Trap	33	73	0.14	0.00	2.5	0.4	-26.6	0.5	148	224
21	JC187-ST-42-43	Trap	31	79	0.17	0.02	2.9	0.1	-26.6	0.5	165	193
22	JC187-ST-43-44	Trap	38	89	0.16	0.01	2.8	0.1	-26.7	0.4	154	187
23	JC187-ST-44-45	Trap	38	84	0.18	0.03	3.3	0.2	-26.6	0.5	162	187
24	JC187-ST-45-46	Trap	5	18	0.26	0.01	3.8	0.3	-26.6	0.3	168	226
25	JC187-ST-46-47	Trap	5	14	0.28	0.00	3.9	0.2	-26.7	0.3	166	244
26	JC187-ST-47-48	Trap	6	18	0.29	0.01	4.2	0.3	-26.7	0.4	163	249
27	JC187-ST-48-49	Trap	5	20	0.29	0.02	4.3	0.4	-27.0	0.3	161	257
28	JC187-ST-49-50	Trap	6	23	0.29	0.01	4.5	0.3	-27.0	0.3	164	230
29	JC187-ST-50-51	Trap	5	18	0.30	0.01	4.4	0.3	-27.0	0.3	168	250
30	JC187-ST-51-52	Trap	5	21	0.31	0.01	4.4	0.3	-27.0	0.3	163	230
31	JC187-ST-52-53	Trap	5	18	0.25	0.03	4.0	1.0	-26.9	0.2	161	235
32	JC187-ST-53-54	Trap	5	18	0.31	0.00	4.3	0.3	-26.8	0.5	165	233
33	JC187-ST-54-55	Trap	5	18	0.31	0.02	4.3	0.2	-26.8	0.4	160	220
34	JC187-ST-55-56	Trap	5	17	0.30	0.00	3.9	0.2	-26.8	0.2	160	241
35	JC187-ST-56-57	Trap	5	18	0.29	0.04	4.2	0.2	-26.9	0.3	158	228
36	JC187-ST-57-58	Trap	5	19	0.30	0.07	4.1	0.3	-26.8	0.4	165	216
37	JC187-ST-58-59	Trap	6	21	0.30	0.07	4.2	0.2	-26.8	0.3	162	245
38	JC187-ST-59-60	Trap	6	21	0.33	0.04	4.2	0.2	-26.9	0.3	183	210
39	JC187-ST-60-61	Trap	6	22	0.29	0.02	4.3	0.3	-26.9	0.3	160	223
40	JC187-ST-61-62	Trap	6	21	0.33	0.01	4.4	0.2	-26.8	0.1	153	223
41	JC187-ST-62-63	Trap	6	23	0.34	0.01	4.4	0.2	-26.9	0.3	165	218
42	JC187-ST-63-64	Trap	6	25	0.31	0.04	4.3	0.2	-26.9	0.3	172	216
43	JC187-ST-64-65	Trap	6	24	0.30	0.02	4.3	0.4	-26.9	0.3	149	278
44	JC187-ST-65-66	Trap	7	33	0.31	0.02	4.4	0.3	-27.0	0.3	162	212
45	JC187-ST-66-67	Trap	10	50	0.29	0.04	4.3	0.1	-26.9	0.4	167	204
46	JC187-ST-67-68	Trap	7	34	0.29	0.02	4.3	0.3	-27.0	0.3	167	211
47	JC187-ST-68-69	Trap	8	41	0.29	0.02	4.3	0.1	-26.9	0.4	159	231
48	JC187-ST-69-70	Trap	7	35	0.31	0.01	4.5	0.3	-26.9	0.3	165	212
49	JC187-ST-70-71	Trap	10	42	0.28	0.01	4.1	0.4	-26.9	0.4	155	221
50	JC187-ST-71-72	Trap	14	52	0.27	0.01	4.0	0.4	-26.9	0.4	150	206
51	JC187-ST-72-73	Trap	11	54	0.24	0.01	3.6	0.2	-26.8	0.4	158	212
52	JC187-ST-73-74	Trap	7	29	0.31	0.00	4.2	0.3	-26.9	0.3	177	203
53	JC187-ST-74-75	Trap	8	42	0.30	0.02	4.3	0.3	-27.0	0.3	160	224
54	JC187-ST-75-76	Trap	6	26	0.31	0.02	4.5	0.3	-26.8	0.2	162	217
55	JC187-ST-76-77	Trap	6	26	0.29	0.03	4.1	0.2	-26.9	0.3	163	214
56	JC187-ST-77-78	Trap	6	29	0.31	0.01	4.3	0.2	-26.9	0.3	172	216
57	JC187-ST-78-79	Trap	10	46	0.31	0.03	4.3	0.1	-26.9	0.3	160	226
58	JC187-ST-79-80	Trap	18	62	0.23	0.00	3.5	0.3	-26.9	0.4	165	198

Table 1. Continued.

Sample number	Sample code	Sample type	D_{50} (μm)	D_{90} (μm)	TN (%)		TOC (%)		$\delta^{13}\text{C}$ (‰)		HI ($\text{mg CO}_2 \text{ g C}_{\text{org}}^{-1}$)	OI ($\text{mg HC g C}_{\text{org}}^{-1}$)
					mean	SD	mean	SD	mean	SD		
59	JC187-ST-80-81	Trap	10	51	0.32	0.00	4.6	0.3	-26.9	0.5	162	204
60	JC187-ST-81-82	Trap	6	30	0.32	0.01	4.3	0.6	-26.7	0.4	160	220
61	JC187-ST-82-83	Trap	6	19	0.29	0.03	3.8	0.2	-26.6	0.3	161	211
62	JC187-ST-83-84	Trap	7	22	0.32	0.05	4.1	0.2	-26.8	0.4	161	219
63	JC187-ST-84-85	Trap	6	22	0.32	0.01	4.2	0.2	-26.9	0.3	166	212
64	JC187-ST-85-86	Trap	7	25	0.34	0.01	4.4	0.3	-27.0	0.4	174	209
65	JC187-ST-86-87	Trap	6	25	0.33	0.01	4.4	0.3	-27.1	0.3	171	215
66	JC187-ST-87-88	Trap	6	24	0.32	0.01	4.4	0.3	-27.1	0.4	164	215
67	JC187-ST-88-89	Trap	6	25	0.32	0.01	4.4	0.3	-27.1	0.4	172	239
68	JC187-ST-89-90	Trap	11	56	0.31	0.02	4.2	0.1	-27.0	0.3	167	217
69	JC187-ST-90-91	Trap	6	29	0.30	0.02	4.4	0.3	-26.9	0.4	160	219
70	JC187-ST-91-92	Trap	6	27	0.32	0.01	4.5	0.3	-26.9	0.4	159	302
71	JC187-ST-92-93	Trap	7	36	0.31	0.03	4.3	0.2	-26.9	0.4	165	208
72	JC187-ST-93-94	Trap	6	30	0.30	0.03	4.4	0.2	-26.9	0.3	161	225
73	JC187-ST-94-95	Trap	15	59	0.31	0.03	4.4	0.3	-26.9	0.3	171	208
74	JC187-ST-95-96	Trap	14	60	0.26	0.04	4.2	0.2	-26.8	0.4	156	198
75	JC187-ST-96-97	Trap	12	59	0.11	0.05	1.8	0.1	-26.4	0.5	131	264
76	JC187-ST-97-98	Trap	14	62	0.17	0.00	2.9	0.4	-26.6	0.5	151	218
77	JC187-ST-98-99	Trap	27	80	0.12	0.03	2.1	0.3	-26.3	0.1	134	285
78	JC187-ST-99-100	Trap	32	77	0.15	0.01	2.4	0.1	-26.6	0.5	171	404
79	MC05-0–10cm	Multi-core	4	20	0.27	0.02	4.0	0.7	-26.4	0.5	154	189
81	MC05-20–30cm	Multi-core	9	34	0.30	0.01	4.3	0.4	-26.7	0.4	165	162
83	MC05-40–50cm	Multi-core	13	55	0.26	0.01	3.7	0.1	-26.8	0.3	145	159
84	MC06-40–50cm	Multi-core	8	26	0.26	0.01	3.7	0.3	-26.3	0.5	140	161
85	MC06-20–30cm	Multi-core	6	23	0.20	0.01	3.3	0.5	-26.3	0.4	154	168
86	MC06-0–10cm	Multi-core	4	19	0.25	0.02	3.5	0.5	-26.4	0.4	158	160
87	MC07-top	Multi-core	8	28	0.27	0.01	3.4	0.4	-25.9	0.4	159	162
88	MC07-20–30cm	Multi-core	11	40	0.29	0.01	3.5	0.4	-25.9	0.5	161	155
89	MC07-40–50cm	Multi-core	7	22	0.26	0.01	3.3	0.2	-25.7	0.5	146	161
90	MC03-0–10cm	Multi-core	10	35			3.9	0.3	-26.5	0.7	122	198
91	MC03-40–50cm	Multi-core	6	17			3.4	0.7	-26.4	0.6	178	198
92	MC04-0–10cm	Multi-core	4	22			4.7	0.6	-27.1	0.6	154	206
93	MC04-30–40cm	Multi-core	3	20			5.1	0.4	-26.9	0.6	163	202

up to 400 °C are expressed in milligrams of CO_2 per gram of sample. Dividing the amount of HC and CO_2 by the total organic carbon content (TOC) of each sample provides the hydrogen index (HI in milligrams of HC per gram of TOC) and the oxygen index (OI in milligrams of CO_2 per gram of TOC), respectively. HI and OI can inform on the type of organic matter (e.g., terrestrial, oxidized, marine) in a HI versus OI diagram (Baudin et al., 2015, 2017).

3.4 Organic carbon flux calculations

Combining the timing and durations of turbidity currents from the ADCP data with sediment properties and carbon content measured in the trap, we calculated transit organic carbon fluxes for our study period as follows. First, we derived sedimentation rates (i.e., rates at which particles were falling in the trap) for periods when turbidity currents were active and for periods when tides were dominant. This could be achieved by matching the date and time of four scheduled disks that fell in the sediment trap with the correspond-

ing date and time of flows recorded by the ADCP. To refine rates related to periods of active turbidity currents, the base of very fine-sand layers identified in the trap (e.g., at 99, 70, and 39 cm depth of the trap) were correlated to the start of turbidity currents 1, 2, and 6. Once sedimentation rates were known for each period, we used Eq. (1) to derive a specific organic carbon flux per sample, expressed in grams of organic carbon per square meter per day ($\text{g C}_{\text{org}} \text{ m}^{-2} \text{ d}^{-1}$).

$$\text{Flux C}_{\text{org}} = \frac{\text{TOC} \cdot (1 - \varphi) \cdot \rho_{\text{quartz}} \cdot \text{SR}}{\text{SA}_{\text{funnel}}/\text{SA}_{\text{liner}}} \quad (1)$$

Here TOC is the total organic carbon content measured by elemental analysis (see Sect. 3.3), SR is the sedimentation rate obtained as explained above, φ is the porosity of the sediment fallen in the trap measured by the multi-sensor core logger (Fig. S1), and ρ_{quartz} is the density of quartz (2.65 g cm^{-3}). SA_{liner} is the surface area of the core liner (diameter of 6.3 cm) containing the trapped particles, and $\text{SA}_{\text{funnel}}$ is the surface area of the open top funnel (diameter of 25 cm).

Table 2. Radiocarbon measurements of 30 selected samples. $F^{14}R$ was calculated using the radiocarbon age of the atmosphere in 2019 ($F^{14}C = 1.019 \pm 0.0004$; Hua et al., 2022).

Sample code	NEIF reference number	$F^{14}C$		$\delta^{13}C$ (‰)	$F^{14}R$	
		mean	SD		mean	SD
JC187-ST-25-26	SUERC-107302	0.920	0.004	-26.693	0.902	0.004
JC187-ST-30-31	SUERC-107307	0.914	0.004	-26.808	0.896	0.004
JC187-ST-32-33	SUERC-107308	0.922	0.004	-26.830	0.904	0.004
JC187-ST-36-37	SUERC-107309	0.925	0.004	-26.745	0.907	0.004
JC187-ST-40-41	SUERC-107310	0.923	0.004	-26.814	0.905	0.004
JC187-ST-43-44	SUERC-107311	0.949	0.004	-26.195	0.930	0.004
JC187-ST-45-46	SUERC-107312	0.913	0.004	-26.539	0.895	0.004
JC187-ST-57-58	SUERC-107316	0.931	0.004	-26.878	0.913	0.004
JC187-ST-65-66	SUERC-107317	0.964	0.004	-26.994	0.945	0.004
JC187-ST-68-69	SUERC-107318	0.952	0.004	-26.807	0.934	0.004
JC187-ST-72-73	SUERC-107319	0.937	0.004	-26.960	0.919	0.004
JC187-ST-75-76	SUERC-107320	0.950	0.004	-26.870	0.932	0.004
JC187-ST-77-78	SUERC-107321	0.950	0.004	-26.893	0.932	0.004
JC187-ST-79-80	SUERC-107322	0.940	0.004	-26.947	0.922	0.004
JC187-ST-81-82	SUERC-107326	0.933	0.004	-26.692	0.915	0.004
JC187-ST-85-86	SUERC-107327	0.938	0.004	-26.975	0.920	0.004
JC187-ST-89-90	SUERC-107328	0.953	0.004	-27.020	0.935	0.004
JC187-ST-91-92	SUERC-107329	0.944	0.004	-26.931	0.926	0.004
JC187-ST-95-96	SUERC-107330	0.912	0.004	-26.701	0.894	0.004
JC187-ST-96-97	SUERC-107331	0.811	0.004	-26.050	0.795	0.004
JC187-ST-98-99	UCIAMS-274854	0.846	0.007		0.829	0.007
JC187-MC05-0-10	SUERC-108883	0.949	0.004	-25.407	0.930	0.004
JC187-MC05-40-50	SUERC-108884	0.944	0.004	-26.013	0.925	0.004
JC187-MC06-0-10	SUERC-108889	0.930	0.004	-25.683	0.912	0.004
JC187-MC07-0-10	SUERC-108890	0.924	0.004	-25.755	0.906	0.004
JC187-MC07-20-30	SUERC-108891	0.926	0.004	-25.758	0.908	0.004
JC187-MC03-0-10	SUERC-108892	0.812	0.004	-26.300	0.796	0.004
JC187-MC03-30-40	SUERC-108893	0.807	0.004	-26.197	0.791	0.004
JC187-MC04-0-10	SUERC-108894	0.968	0.004	-26.734	0.949	0.004
JC187-MC04-30-40	SUERC-108898	0.960	0.004	-26.697	0.941	0.004

4 Results

4.1 Observations of particle transport in the submarine Congo Canyon

Our eight studied turbidity current events have internal velocity magnitudes of maximum 1.5 m s^{-1} (Fig. 2) and frontal velocities of up to 4 m s^{-1} based on transit times between moorings (Talling et al., 2022). Flow durations varied between $< 1 \text{ d}$ (e.g., Flow 4 in Fig. 2) and $> 3 \text{ d}$ (e.g., Flows 1 and 6 in Fig. 2a and c). Flow heights reached $> 32 \text{ m}$ (i.e., height of the ADCP instrument above canyon floor) in four of the eight observed turbidity currents. We note that our eight studied flows have shorter run-out distances and slower speeds compared to the January 2020 event, which ran out for $> 1000 \text{ km}$ down canyon (Talling et al., 2022). This latter flow broke our M9 mooring line so it could be captured in neither the ADCP nor the sediment trap.

Along-canyon velocity (V_{along} ; Figs. 3, S2, and S3 in the Supplement) computed before and between turbidity current events, reveals that there is an oscillatory continuous-flow regime with currents alternating between net upslope (negative values) and downslope (positive values) directions and with speeds ranging from -0.15 to $+0.15 \text{ m s}^{-1}$. For this background “oscillatory flow”, the residual V_{along} current direction points upslope as illustrated by the hodographs computed for the arrays 5 and 30 m above the seabed (Fig. 4). Across-canyon velocity (V_{across}) oscillates between -0.15 (SW direction) and $+0.15$ (NE direction) m s^{-1} but has little influence on the net current trajectory compared to V_{along} and shows no pattern or dominant frequencies. This oscillatory flow is homogenous through the observed water column (i.e., 30 m), as demonstrated by constant values in both V_{along} and V_{across} through the ADCP measured range (32 m; Figs. 3a, S2 and S3). The CTD data collected when there was no turbidity current activity also reveal that salinity, oxygen, and turbidity values are homogenous and rela-

tively high in the confined water column, compared to intermediate unconfined waters (Fig. 5). The frequency analysis reveals one main frequency of 12.5 h (Fig. 3), corresponding to semi-diurnal tides in the Congo River estuary. Internal tides are internal gravity waves at tidal frequency, generated by the interaction of the tidal currents with the seafloor topography (e.g., Garrett and Kunze, 2007). These feature sheared vertical structures of currents and pressure. With the ADCP measurements alone, we cannot unambiguously attribute the semidiurnal signal to internal tides, although they likely dominate the signal. We thus call the observed oscillations confined within the canyon morphology “tides” in the following text.

Sedimentary deposits associated with tides and turbidity currents measured by the ADCP are recorded in the sediment trap deployed just below the ADCP instrument. The trap contains a 1.2 m thick sedimentary succession made of mud (mean $D_{90} = 22 \mu\text{m}$) and coarse-silt to very fine-sand layers (mean $D_{90} = 51 \mu\text{m}$; Fig. 6). These silt to very fine-sand layers are between 2 and 7 cm thick. The disks enable us to correlate the base of the fine-sand layers with the turbidity current events detected by the ADCP (Fig. 6a and b). The trap was deployed 30 m above the seabed, and hence particles transported closer to the seabed could not be retrieved. Despite this, the base of the silt to very fine-sand event layers observed in the trap are sharp and overlain by a fining-upward succession (Fig. 6c), features typical of the deposits of turbidity currents (i.e., Bouma sequence; Bouma, 1962). Turbidity currents that were detected close together in the ADCP data (e.g., events 2 to 5 and events 6 to 8) appear as multi-pulses in the grain size analysis measured on the trapped sediments (Fig. 6c).

Finally, sedimentary facies observed in the five multi-cores from the canyon thalweg, terrace levels, and channel correspond to homogenous muds without any structure such as laminations. Samples collected in these multi-cores have a mean D_{90} of $28 \mu\text{m}$ and are thus of similar grain size to the muds observed in the trap (Fig. 7a and b).

4.2 Organic carbon composition in trapped and seabed sediments

Sediment in the trap shows a mean TOC content of $4.0\% \pm 0.6\%$ ($n = 78$), with a minimum and maximum TOC of 1.8% and 4.6%, respectively (Fig. 6d). TOC content in the trap appears to be controlled by sediment grain size, with sandy samples ($D_{90} > 63 \mu\text{m}$) having lower TOC (mean = $2.6\% \pm 0.4\%$, $n = 9$) compared to muddy samples (mean = $4.2\% \pm 0.4\%$, $n = 69$). TOC measured at the base of the very fine-sand event layers is thus relatively low compared to the top of each event layer (Fig. 6d). Homogenous muds below sandy event beds show a slight decrease in TOC content with time at equal D_{50} and slightly decreasing D_{90} (e.g., from 36 to 30 cm, TOC = $4.5\% \pm 0.3\%$ to $3.8\% \pm 0.3\%$ and from 83 to 75 cm, TOC = $4.4\% \pm 0.3\%$

to $3.8\% \pm 0.2\%$ in Fig. 6d). TOC measured on the multi-core muddy samples from the surficial canyon seabed reveal a slightly lower organic carbon content (TOC = $3.6\% \pm 0.4\%$, $n = 11$, Fig. 6a) compared to the muddy sediment observed in the trap. TOC values from the distal channel seabed multi-cores (TOC = $4.3\% \pm 0.7\%$, $n = 4$) are similar to those in the trap. Overall, there is a negative relationship between TOC and grain size in both the trapped and seabed samples (Fig. 7a).

All trap and multi-core samples analyzed here contain organic carbon of terrestrial origin based on rather constant low carbon stable isotope ratios ($\delta^{13}\text{C} = -26.8\text{‰} \pm 0.3\text{‰}$, $n = 91$), high C/N ratios (17.1 ± 1.4 , $n = 87$), and low hydrogen and oxygen indexes (HI = $161 \pm 9 \text{ mg HC per g TOC}$; OI = $220 \pm 34 \text{ mg CO}_2 \text{ per g TOC}$; $n = 91$). Radiocarbon measurements ($F^{14}\text{R}$ values) conducted on 30 samples from both the trap and multi-cores (in both canyon and channel) range between 0.791 and 0.949. There is no significant relationship between grain size and radiocarbon isotope composition based on our 30 measurements, although it appears that the four oldest radiocarbon ages ($F^{14}\text{R} = 0.791$ to 0.829) measured in our sample set correspond to trap sandy and distal channel samples (Fig. 7b).

4.3 Organic carbon fluxes

We find that transit fluxes of organic carbon at 30 m above the seafloor in the submarine Congo Canyon range between 5 and $33 \text{ g C}_{\text{org}} \text{ m}^{-2} \text{ d}^{-1}$. Fluxes attributed to turbidity currents are on average 3 to 6 times higher compared to the carbon fluxes related to the background conditions, i.e., not including turbidity currents (Fig. 8). The background hydrodynamical conditions are associated with a net residual flow that is oriented up canyon due to a combination of tidally driven processes, mixing processes, and the low-frequency circulation (e.g., Lahaye et al., 2019). This residual flow retains particles within the canyon before turbidity currents transport particles with a net transit direction oriented downstream towards the deep sea. We note that our sediment fluxes are estimated at 30 m above the bed and may thus differ from overall sediment fluxes down the canyon, especially due to vertical variations in sediment concentrations and velocities expected in turbidity currents, as discussed in Sect. 5.1.

5 Discussion

5.1 What are the hydrodynamic processes controlling the transport of particulate organic carbon in the submarine Congo Canyon?

Two processes drive the fate of sediment and particulate organic carbon through the submarine Congo Canyon from the Congo River estuary to the deep-sea fan (Fig. 9): downslope turbidity currents and a background circulation dominated by tidal currents.

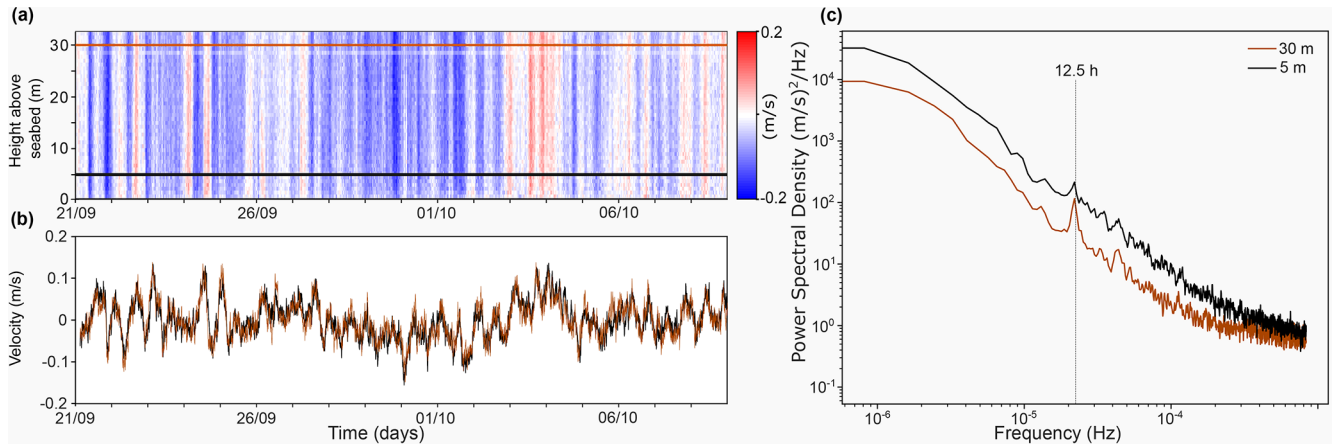


Figure 3. Velocity along the canyon (V_{along}) and frequency analysis at mooring M9 at 2170 m water depth for the period 21 September to 10 October 2019 when there was no turbidity current activity (see Fig. 2a for context). **(a)** Time series of V_{along} between 21 September and 10 October 2019. The horizontal brown and black lines indicate the heights above the seabed of the velocity time series displayed in **(b)**. **(b)** V_{along} speeds at 5 (black line) and 30 m (brown line) above the canyon floor. **(c)** Power spectral density computed for the whole time series (21 September 2019 to 15 January 2020) at 5 (black line) and 30 m (brown line) above the seafloor. Here, 12.5 h indicates the time period of the first frequency peak observed (frequency = 1/time).

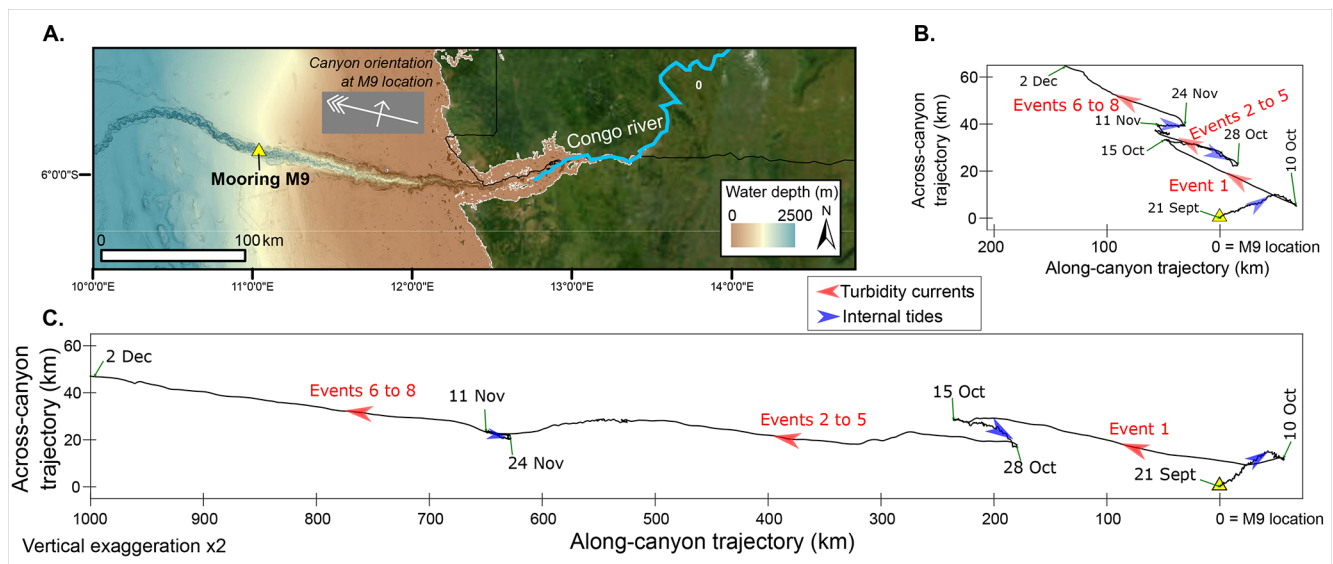


Figure 4. **(a)** Location of the moored ADCP (mooring M9) deployed in the Congo Canyon at 2190 m water depth. The aerial image of the Congo River mouth is taken from © Google Earth. **(b)** Hodograph showing residual currents measured at the mooring M9 location 30 m above the seabed. **(c)** Hodograph showing residual currents measured at mooring M9 location 5 m above the seabed. The start and end dates of turbidity current series recorded by the ADCP are marked. Red arrows show a downslope trajectory due to turbidity currents, whereas blue arrows show a net upslope trajectory due to internal tides.

Turbidity currents occur 35 % of the time during monitoring periods in the upper submarine Congo Canyon (Azpiroz-Zabala et al., 2017; Simmons et al., 2020; Talling et al., 2022). Through our study, we show that turbidity currents carry particulate organic carbon at a much higher transit flux (3 to 6 times higher, Fig. 8) compared to the transit flux associated with background circulation dominated by tidal currents, at least for relatively small turbidity currents (see

Azpiroz-Zabala et al., 2017; Talling et al., 2022), at a height of 30 m above the bed (Fig. 2a). Our calculated fluxes should not be regarded as sedimentation rates as they represent a settling flux in the sediment trap, which greatly exceeds the settling rate on the seabed (Gardner, 1980), particularly in highly active submarine canyons. Despite this, the particulate organic carbon transit flux due to turbidity currents is likely underestimated because the height of our sediment trap (30 m

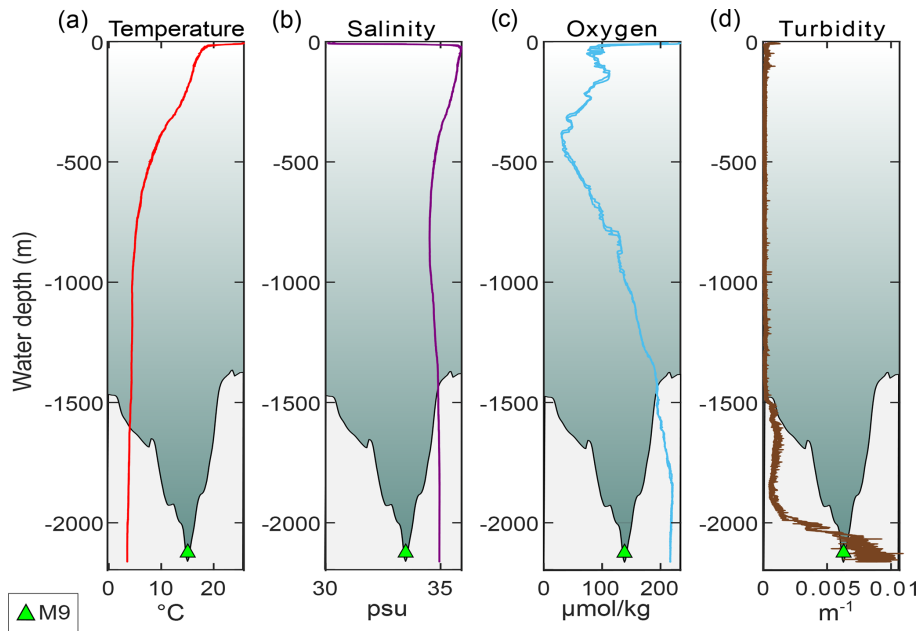


Figure 5. Conductivity–temperature–depth (CTD) profiler and turbidity sensor data collected on 21 September 2019 at the mooring M9 location at 2170 m of water depth (see Fig. 1 for location) outside of turbidity current activity. The grey line shows a cross section of the across-canyon morphology at the mooring location.

above the seabed) did not allow coarse sands transported at the base of turbidity currents to be collected. The base of turbidity currents (e.g., 0 to 5 m above the seabed) are usually characterized by the flow's highest velocities and sediment concentrations (Kneller and Buckee, 2000; Sequeiros et al., 2009). These higher velocities can carry larger fresh vegetation debris associated with coarser sands (McArthur et al., 2016). For example, event beds containing a large amount of vegetation debris (TOC of up to 11.3%) associated with medium sands (in a muddy matrix) were reported in some piston cores collected in the Congo Canyon and channel (Baker et al., 2024). Furthermore, vegetation-rich sandy turbidites were observed in submarine canyons deposits elsewhere (e.g., Saller et al., 2006; Lee et al., 2019; Hage et al., 2020), supporting our hypothesis. We note that far more sediment may be carried in much larger and infrequent canyon-flushing flows, as occurred in January 2020, breaking our mooring line (Fig. 2). Just two canyon-flushing turbidity currents in 2020 likely carried $\sim 2.65 \text{ km}^3$ of sediment down the Congo Canyon, which is equivalent to 19%–33% of the total annual sediment flux from all of the world's rivers (Talling et al., 2022). Those much larger canyon-flushing flows may have recurrence intervals of 20–50 years (Talling et al., 2022).

Between episodic turbidity currents, we observe a background oscillatory flow with dominant frequencies related to semi-diurnal tides (12.49 h of period) at a speed of up to 0.15 m s^{-1} directed both up and down canyon. These tidal currents affect the measured (32 m) water column homoge-

nously and show a residual current direction that points upslope (Figs. 3, 5 and 6). Tidal currents and their residual upslope flux were described previously in the Congo distal submarine channel at 4070 m water depth based on current meter data at 6 m above the seabed but with slightly lower speeds (mean of 2.5 cm s^{-1} ; Vangriesheim et al., 2009) compared to our measurements. The V-shaped morphology of submarine canyons and channels appears to enhance the vertical mixing up and down canyon compared to the higher open-water column. Currents associated with tides are thus morphologically confined closer to the canyon thalweg (i.e., tides are internal to the canyons), as observed for example in the Logan (eastern Canada) and Cassidaigne (Mediterranean Sea) submarine canyons (Li et al., 2019; Brun et al., 2023). Confined mixing by tides keeps the fine particulate organic carbon delivered via the top part (i.e., slower-moving) of turbidity currents in suspension. This is attested by the presence of muds in the sediment trap between the turbidity current event beds, falling at rates of 0.7 to 1.1 cm d^{-1} during periods dominated by tides (Figs. 6 and 8b). Seabed deposits of tides have been described in the literature as being composed of laminated muddy sand to silt (e.g., Normandeau et al., 2024). Such laminations cannot be produced in a sediment trap and are thus not observed in our trapped succession (Fig. 6). The upper 30 cm of the canyon and channel seabed were retrieved in the multi-cores, which do not reveal laminations either (at least to the naked eye). The flushing and reworking of sediment by turbidity currents likely prevent any fine-scale laminated structures from being preserved on the seabed, confirming

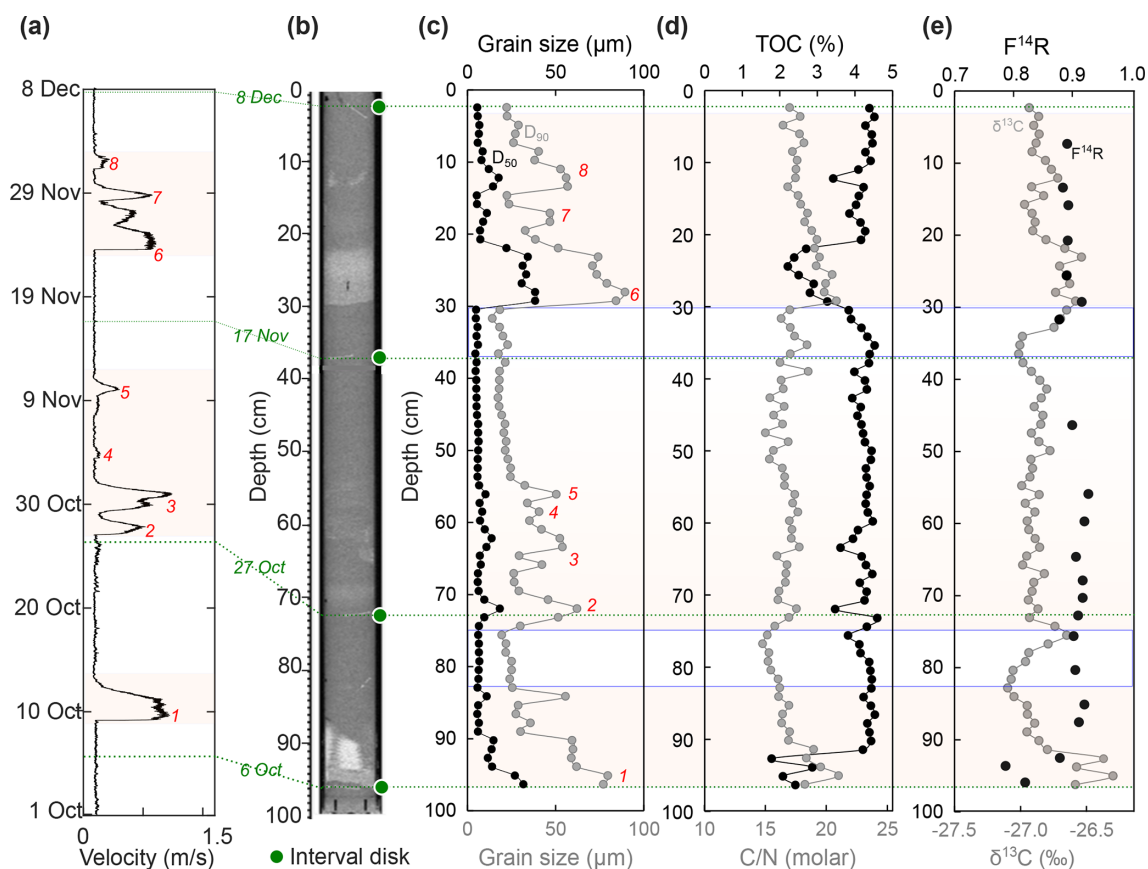


Figure 6. Overview of the data collected from the ADCP and the sediment trap. **(a)** Velocity magnitude measured by the ADCP averaged over 30 m above the seabed. Flows recorded in ADCP data (Fig. 2) are numbered. **(b)** X-ray of the sediment succession retrieved from the sediment trap deployed on the same mooring as the ADCP 30 m above the canyon floor. **(c)** Grain size measurements made on samples taken every 1 cm in the trapped succession. The black line represents the grain size median (D_{50}). The grey line represents the grain size D_{90} . **(d)** Total organic carbon content (TOC) and organic carbon over nitrogen ratios (C/N) measured on samples taken every centimeter along the trapped succession. **(e)** Carbon stable isotope ratio ($\delta^{13}\text{C}$) and relative ^{14}C enrichment (relative to year 2019; $F^{14}\text{R}$, Soulet et al., 2016) measured on samples taken every centimeter along the trapped succession. The yellow rectangles in the background highlight periods when turbidity currents are active.

again that turbidity currents are the dominant hydrodynamic process in the submarine Congo Canyon.

In summary, turbidity currents rapidly move sediment and particulate organic carbon downslope in one go at a transit flux that we estimate to be at least 3 to 6 times higher compared to the flux induced by the background circulation when tides dominate. It then appears that the fine-grained material flushed episodically into the canyon by the top part of turbidity current and the turbidity current tail may then be kept in suspension and mixed in the canyon water column by tides. This material will remain in the canyon until turbidity currents with a net downstream transport direction transfer the particles all the way through the canyon to the deep sea. The impact of these combined hydrodynamic processes on organic carbon composition (i.e., isotopic composition and Rock-Eval indexes) is further discussed in the next section.

5.2 How does carbon transiting the canyon compare with carbon composition in the river and deep-sea fan?

The trap and seabed sediments in our study show similar carbon isotopic (both $\delta^{13}\text{C}$ and ^{14}C) compositions to those previously sampled in the Congo River (Figs. 7b and 9; Spencer et al., 2012; Hemingway et al., 2017), implying that the material transiting in the submarine canyon and channel is entirely derived from the river. Total organic carbon contents measured in the Congo River suspended sediment averages $6.1\% \pm 1.0\%$ with maximum TOC of 8.9% (Mariotti et al., 1991; Coynel et al., 2005; Hemingway et al., 2017). This is higher than the average TOC measured in our canyon trap (TOC = $4.0\% \pm 0.6\%$), yet the Congo River bedload was not considered in those previous studies and could likely decrease the river's average TOC. Furthermore, TOC of up to 11.3% was measured in vegetation-rich muddy sand deposits

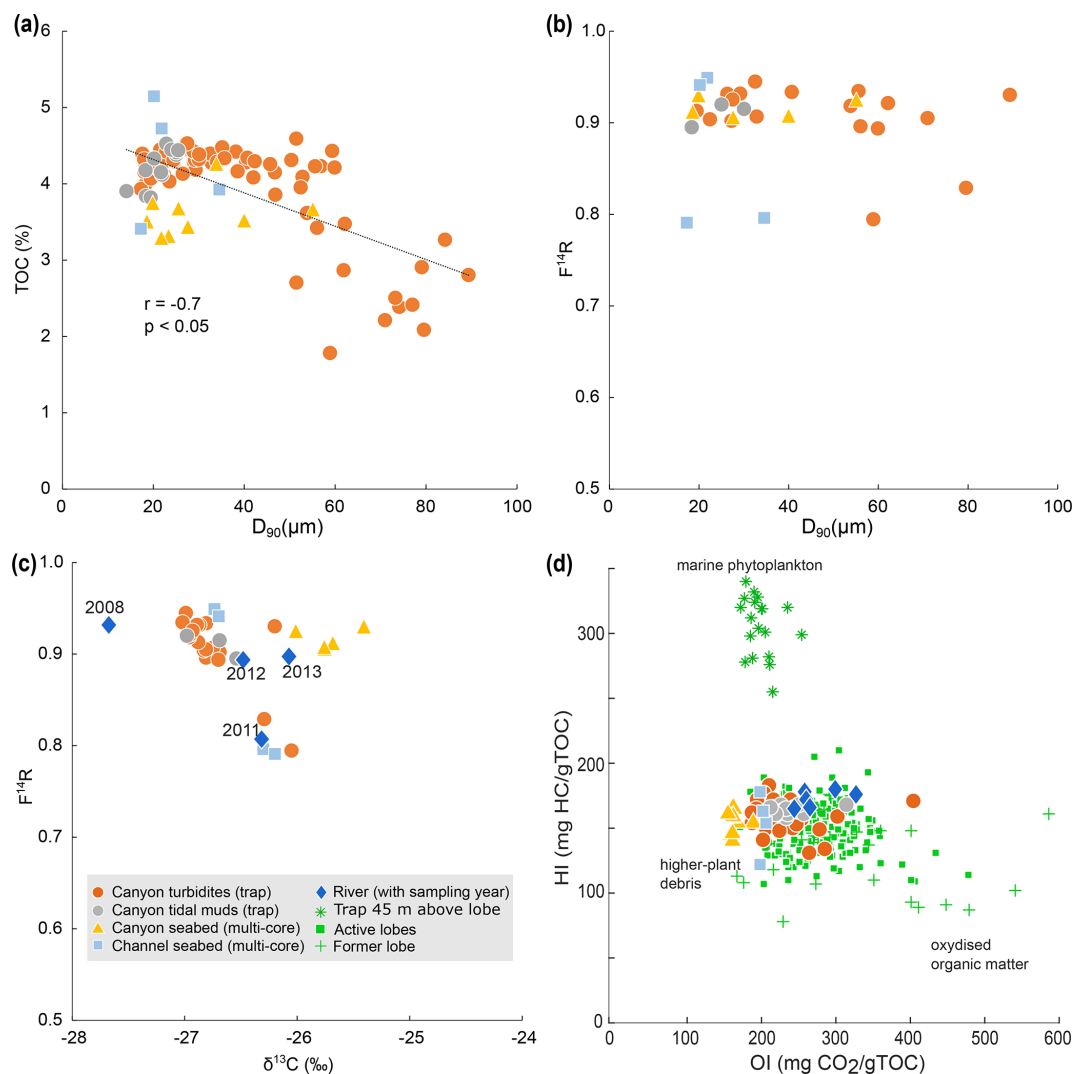


Figure 7. Measurements made on trap and seabed samples collected in the Congo Canyon and Channel, with previous data from Congo River and lobe. **(a)** Total organic carbon content (TOC) against grain size D_{90} in micrometers. **(b)** Relative ^{14}C enrichment (relative to year of sample collection in 2019; $F^{14}\text{R}$) against D_{90} in micrometers. **(c)** Relative ^{14}C enrichment (relative to year of sample collection in 2019; $F^{14}\text{R}$) against carbon stable isotope ratios ($\delta^{13}\text{C}$). River data are taken from Spencer et al. (2012) and Hemingway et al. (2017) and are averaged between samples collected in 1 year (labeled 2008, 2011, 2012, and 2013). **(d)** Hydrogen index against oxygen index derived from Rock-Eval pyrolysis and oxidation. Lobe data are taken from Baudin et al. (2017).

in piston sediment cores retrieved from the submarine Congo Canyon axis (Baker et al., 2024). Such vegetation-rich deposits are not present in our canyon trap that is located 30 m above the seabed.

Carbon stable isotopes and Rock-Eval index compositions (HI and OI) are also similar between our submarine canyon and channel samples and previously reported seabed samples retrieved in distal lobes (Figs. 7d and 9; Baudin et al., 2010, 2017; Stetten et al., 2015). This suggests that organic carbon is efficiently flushed to deep-sea lobes; however, this hypothesis needs to be further corroborated by radiocarbon measurements on particulate organic carbon deposited in lobes. Our canyon and channel samples show a different carbon

composition compared to sediment retrieved from a trap previously deployed 45 m above the seabed at 4779 m water depth (Rabouille et al., 2017a; Baudin et al., 2017). This trap shows higher $\delta^{13}\text{C}$, higher HI, and lower OI compared to our canyon and channel samples (Figs. 7d and 9). The organic carbon composition of the distal trap corresponds to marine organic carbon sinking from the photic zone in the water column at 45 m above the seabed. This marine signature was not found in the seabed sediments beneath the same trap, probably due to rapid degradation of marine organic matter in the first few centimeters below the seabed (Treignier et al., 2006; Baudin et al., 2017). There is also no evidence for the presence of such marine organic carbon in our canyon trap and

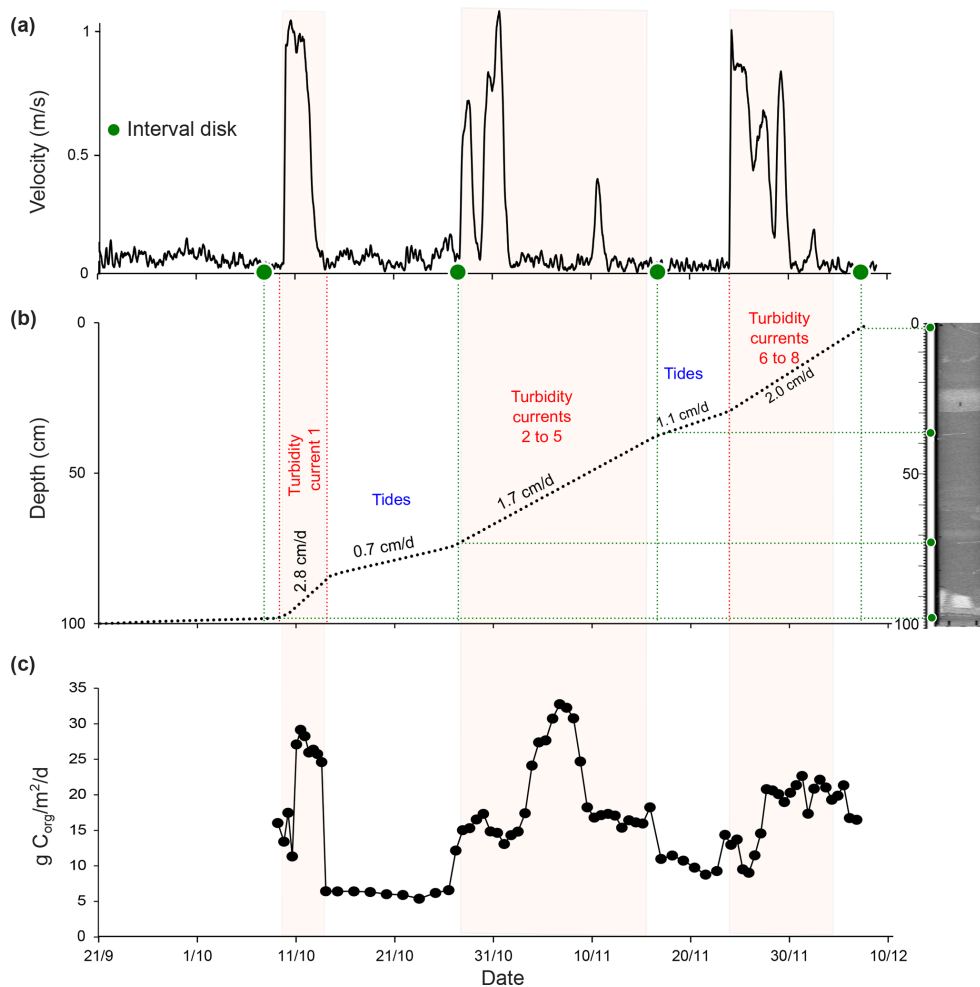


Figure 8. (a) Velocity magnitude measured by the ADCP averaged over 30 m above the seabed. (b) Apparent sediment accumulation rates (in cm d^{-1}) calculated in the sediment trap and X-ray of the trapped core. (c) Transit fluxes of particulate organic carbon (in $\text{g C}_{\text{org}} \text{m}^{-2} \text{d}^{-1}$) calculated based on (b), total organic carbon contents (Fig. 6c), and sediment properties measured in the trapped sediment by multi-sensor core logging.

seabed samples, probably because terrestrial organic carbon sourced from the Congo River brought in by turbidity currents is dominant and dilutes the marine signal in the canyon. Turbidity currents were not recorded in the distal sediment trap (Rabouille et al., 2017a; Baudin et al., 2017) as flows reach the distal channel-lobe transition zone at a much lower frequency (every 6 to 10 years; Dennielou et al., 2017) compared to the upper canyon where flows occur several times per year (e.g., Fig. 2a).

Overall, the isotopic composition and total content of particulate organic carbon in the Congo Canyon during our studied period is similar to that reported in both the Congo River (Spencer et al., 2012; Hemingway et al., 2017) and the deep-sea lobe seabed (Baudin et al., 2010, 2017; Stetten et al., 2015). Both tides and episodic turbidity currents thus do not seem to significantly affect the composition of riverine particulate organic carbon transiting through the sub-

marine canyon towards the deep sea (Fig. 9). Further, tides appear to mix fine particulate organic carbon, leading to relatively homogenous stable carbon and radiocarbon isotope composition in the trap (Fig. 6). Despite this overall homogenous trend, we note that carbon contents in the tidal muds show a slight decreasing trend ($\text{TOC} = 3.8\% \pm 0.3\%$, $n = 12$) below coarser deposits and compared to muds associated with turbidity current events ($\text{TOC} = 4.2\% \pm 0.4\%$, $n = 69$; Fig. 6d) in the trap. This occurs at relatively constant grain size D_{50} ($D_{50} = 5.9 \pm 0.6 \mu\text{m}$, $n = 12$) but slightly decreasing D_{90} (e.g., from 24 to 18 μm between 37 and 30 cm in the trap; Fig. 6d). This subtle decrease in TOC in the tidal muds can be explained by two reasons. First it could represent loss of organic matter (up to $\sim 10\%$ total loss in the tidal muds), which could occur during suspension in the canyon where the water column is oxygenated as shown in the CTD data (up to ~ 500 m above the seabed; Fig. 5). How-

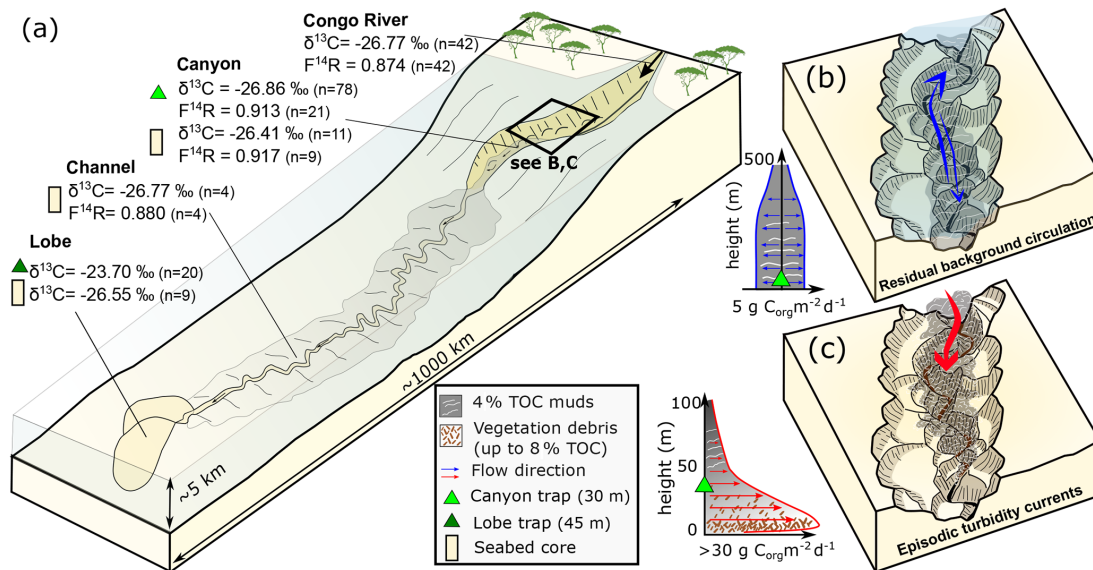


Figure 9. Summary of particulate organic carbon transport in the Congo Submarine Fan. (a) Schematic of the Congo River submarine canyon to deep-sea fan system (modified from Babonneau, 2003). Carbon stable isotopes ($\delta^{13}\text{C}$) and radiocarbon ($F^{14}\text{R}$) compositions are shown for each part of the fan, with river data taken from Spencer et al. (2012) and Hemingway et al. (2017) and lobe data taken from Baudin et al. (2017). (b) A 3D illustration of the residual up-canyon current during background conditions dominated by tides in the canyon with a net residual flow that is directed up canyon and an idealized velocity profile showing the oscillations with a downslope (positive values) and upslope direction (negative values) as observed in Fig. 3a and b. Particulate organic-carbon-rich muds (up to 4% total organic carbon, TOC) are also represented in grey. (c) A 3D illustration of a turbidity current transporting particulate organic carbon down canyon, and idealized velocity profile of a turbidity current showing coarse vegetation debris at the base of the flow and carbon-rich muds within the top of the flow. Carbon flux (in $\text{g C}_{\text{org}} \text{ m}^{-2} \text{ d}^{-1}$) corresponds to the estimated transit flux based on the sediment trap at 30 m above the seabed.

ever, high rates of organic matter degradation are known for fresh marine organic matter, rather than terrestrial organic matter (Middelburg, 1989; Prahl et al., 1997). Second, the decrease in TOC in tidal muds could also be explained by hydrodynamic sorting whereby free organic matter (i.e., non-mineral organic carbon) settles in the water column together with silty to sandy particles. This second hypothesis is supported by a slight decrease in the grain size D_{90} curve in the tidal muds (Fig. 6c and d), implying there is no loss of total organic carbon content at a given grain size.

5.3 How does carbon transport in the submarine Congo Canyon compare with other submarine canyons?

It is challenging to directly monitor sediment transport in submarine canyons due to difficulty of access and the potential damage caused to measuring instruments by powerful flows (e.g., Khrifounoff et al., 2003; Sumner and Paull, 2014). However, advances in tools used to measure sediment transport have enabled detailed direct observations in a few canyons globally (Puig et al., 2014; Liu et al., 2016; Paull et al., 2018; Clare et al., 2020; Talling et al., 2023). Hydrodynamic processes such as turbidity currents and tides have been reported in canyons elsewhere but sometimes with different flow properties compared to those in the Congo

Canyon. Turbidity current frontal speeds can vary between $< 0.5 \text{ m s}^{-1}$ (e.g., Cassidaigne canyon, Brun et al., 2023) and $> 19 \text{ m s}^{-1}$ (e.g., Grand Banks, Heezen and Ewing, 1952). Flow durations of several days in the Congo Canyon are by far the longest flow durations yet observed, with other flows lasting for a few minutes to hours (e.g., Paull et al., 2018; Heijnen et al., 2022). Turbidity currents in the upper Congo Canyon also occur for 35% of the time during monitoring experiments, which is a far higher fraction than in other monitored systems (Talling et al., 2023). Oscillatory flows due to tides are relatively slow in the Congo Canyon ($< 0.15 \text{ m s}^{-1}$). In other settings, the maximum speed of tides can reach 1 m s^{-1} (e.g., Nazaré Canyon, Masson et al., 2010; Bay of Biscay canyons, Mulder et al., 2012; Guistrennec-Faugas et al., 2020; Gaoping Canyon, Liu et al., 2016; Monterey Canyon, Maier et al., 2019; Cassidaigne Canyon, Brun et al., 2023; Whittard Canyon, Heijnen et al., 2022).

In contrast to the growing number of studies reporting observations of sediment transport in submarine canyons, the impact of hydrodynamic processes on carbon composition in submarine canyons is poorly constrained. A few studies compared particulate organic carbon composition in traps and seabed sediments in submarine canyons (e.g., Kao et al., 2014; Liu et al., 2016; Maier et al., 2019). In a similar way to the Congo Canyon, trap and seabed sediments in the Gaoping

Canyon, offshore Taiwan, include particulate organic carbon dominated by inputs from the Gaoping River, whose mouth is very close to the canyon head (Kao et al., 2014). The efficient transport of this terrestrial organic carbon is also controlled by episodic downslope turbidity currents, with tides with a net up-canyon direction also occurring, but these tides are much faster (1 m s^{-1}) compared to the Congo Canyon (Liu et al., 2016). These processes transport a mix of coarse, plant-derived organic matter, soil organic matter, and a large component of rock organic carbon (Hilton et al., 2012). Unlike the Congo and Gaoping canyons, Monterey Canyon is not directly fed by a river, but its head is located next to the shoreline. Particulate organic carbon composition in the Monterey Canyon trap samples is associated with fast (up to 1 m s^{-1}) tidal currents and comprises a mixture of marine and terrestrial carbon (Maier et al., 2019). This trap composition contrasts with seabed samples collected in Monterey Canyon that are dominated by terrestrial carbon brought by turbidity currents (Maier et al., 2019). Thus, the marine organic carbon seen in the Monterey trap samples is not preserved on the seabed over long timescales, as seen for distal lobe areas in the Congo Fan by Baudin et al. (2017).

Particulate organic carbon concentrations in Congo Canyon sediments are very high ($\text{TOC} = 4.0 \% \pm 0.6 \%$) compared with trapped sediment in the Monterey Canyon ($\text{TOC} = 1.9 \% \pm 0.3 \%$; Maier et al., 2019) and the Gaoping Canyon sediments ($\text{TOC} = 0.5 \% \pm 0.3 \%$; Kao et al., 2014). In the case of the Gaoping Canyon, the difference from the Congo Canyon relates to the starkly different geomorphic setting of the river input basins. In Taiwan, short, steep, and small mountain catchments have rapid erosion rates, producing high rates of terrestrial organic carbon transfer but a low overall TOC due to the deep erosion depth and clastic sediment input (Hilton et al., 2012). In contrast, the Congo Basin drains vast lowland regions before entering the ocean, with high terrestrial productivity and the presence of tropical peatlands (Coynel et al., 2005). Here, erosion processes do not typically mobilize unweathered rocks, and thicker soils can be sources for the particulate organic carbon load (Hemingsway et al., 2017). Overall, the rates of particulate organic carbon transfer per unit catchment area are lower in the Congo River than in Taiwanese rivers (Galy et al., 2015), but the percentage of TOC in the river sediments and the total fluxes are much higher. Monterey Canyon represents an intermediate end-member. There, small catchments deliver sediment and particulate organic carbon to the coastal zone, but the canyon itself is not tightly connected to any river. Higher percentages of TOC in that setting reflect the more important role of marine organic matter (Paull et al., 2006).

More generally, TOC in the submarine Congo Canyon is much higher than the global average of continental shelf sediments (mean $\text{TOC} = 1.63 \%$; van der Voort et al., 2021). Erosion of organic-carbon-rich material in the Congo watershed and subsequent transport by the submarine Congo Canyon and channel appears to occur efficiently and quickly

due to the direct connection between the Congo River estuary and the deep-sea canyon head. Overall, our observations of particulate organic carbon transport in the submarine Congo Canyon reveal that strong hydrodynamic processes in canyons appear to efficiently transport terrestrial particulate organic carbon and export it to the deep sea. We suspect that similar types of hydrodynamic processes in submarine canyons elsewhere, either disconnected from land (e.g., Whittard Canyon, Heijnen et al., 2022) or close to large river systems (e.g., Swatch of No Ground Canyon close to the Ganges–Brahmaputra rivers, French et al., 2018) may also promote the efficient transport of terrestrial organic carbon beyond continental shelves (Talling et al., 2024). Quantification of particulate organic carbon fluxes to the deep sea may thus increase global estimates of ocean carbon burial that are to date mainly focused on coastal areas (Regnier et al., 2022).

6 Conclusion

In this study, we show that the transport of particulate organic carbon in the submarine Congo Canyon is controlled by two hydrodynamic processes. First, fast-moving (up to 8 m s^{-1}) turbidity currents transport river-derived particulate organic carbon to the deep sea for 35 % of the time during our monitoring period (4 months). Second, tidal currents within the confined morphology of the canyon induce a background oscillatory flow at maximum speeds of 0.15 m s^{-1} with an up-canyon residual current direction. Tides constantly mix and oxygenate the canyon water column, keeping fine particulate organic carbon in suspension with up-canyon transport rates of $5 \text{ g C m}^{-2} \text{ yr}^{-1}$. Downslope turbidity currents carry both particulate organic carbon associated with mud and sand at rates of $15\text{--}30 \text{ g C m}^{-2} \text{ yr}^{-1}$, which thus greatly exceeds the sediment transit flux by tides at 30 m above the canyon floor. We infer that this particulate organic carbon flux is even higher within the lower parts of turbidity currents due to density being higher closer to the seabed. Organic carbon isotopic composition appears consistent between the Congo River, the submarine canyon and channel, and the distal deep-sea lobes located 1200 km from the river mouth at 5 km of water depth. Such small changes in age and type of organic carbon imply that transfer of terrestrial particulate organic carbon is efficient from river to upper canyon and then to the deep-sea fan. This leads to some of the highest terrestrial organic carbon contents ever observed in shelf sediments and deep-sea fans globally.

Data availability. Data associated with the paper is available in the open-access repository “SeaNoe” (Hage, 2024).

Supplement. The supplement related to this article is available online at: <https://doi.org/10.5194/bg-21-4251-2024-supplement>.

Author contributions. SH designed the study, analyzed the oceanographic data, performed the measurements for carbon elemental and isotopic compositions, acquired funding for carbon measurements, and wrote the manuscript draft. MLB analyzed the sediment trap (MSCL scanning, X-ray acquisition, description, and grain size measurements), extruded samples from the trap, and contributed significantly to the design and writing of the paper. PJT acquired the NERC funding and led cruise JC187. NB, GS, and BD contributed to the design of the manuscript. NB produced the summary figure. GS analyzed the geochemical data and edited the manuscript. RGH, VG, FB, CR, SS, and SA analyzed and commented on the geochemical data. CV and RSJ analyzed and commented on the oceanographic data. All authors reviewed and agreed on the final version of the manuscript.

Competing interests. The contact author has declared that none of the authors has any competing interests.

Disclaimer. Publisher's note: Copernicus Publications remains neutral with regard to jurisdictional claims made in the text, published maps, institutional affiliations, or any other geographical representation in this paper. While Copernicus Publications makes every effort to include appropriate place names, the final responsibility lies with the authors.

Acknowledgements. Sophie Hage has received funding from the European Union's Horizon 2020 research and innovation programme under a Marie Skłodowska-Curie grant agreement (899546). Megan L. Baker was funded by Leverhulme Trust Early Career Fellowship ECF-2021-566. Peter J. Talling acknowledges UK Natural Environment Research Council (NERC) grants (NE/R001952/1 and NE/S010068/1). Sophie Hage and Bernard Dennielou acknowledge funding from the INSU LEFE programme for the project "TOC-CC". We thank the captain, the crew, and the scientific team of James Cook cruise JC187. We are grateful to Katie Maier (NIWA) for providing advice on how to remove sediment from the trap. We also thank Neil Tunstall (Durham University Geography Laboratories) for designing the necessary equipment and methodology for extruding the trap sediment and Ed Pope (Durham University) for assisting with removing the trap sediment. Finally we thank Philippa Ascough (NEIF radiocarbon facility), Caroline Gauthier (LSCE), Florence Savignac (ISTeP), and Loïc Michel (ULiège) for carbon isotope and Rock-Eval analyses. We thank the three reviewers Miquel Canals, Pere Puig, and Lina Madaj and the Associate Editor Tyler Cyronak for their constructive comments that greatly improved our manuscript.

Financial support. This research has been supported by the EU H2020 Marie Skłodowska-Curie Action (grant no. 899546), the Leverhulme Trust (grant no. ECF-2021-566), the Natural Environment Research Council (grant nos. NE/R001982/1 and

NE/S010068/1), and the Centre National de la Recherche Scientifique, Institut national des sciences de l'Univers (LEFE).

Review statement. This paper was edited by Tyler Cyronak and reviewed by Pere Puig, Miquel Canals, and Lina Madaj.

References

- Anderson, R. Y.: Short term sedimentation response in lakes in western United States as measured by automated sampling, *Limnol. Oceanogr.*, 22, 423–433, <https://doi.org/10.4319/lo.1977.22.3.0423>, 1977.
- Ascough, P., Bompard, N., Garnett, M. H., Gulliver, P., Murray, C., Newton, J.-A., and Taylor, C.: ^{14}C Measurement of Samples for Environmental Science Applications at the National Environmental Isotope Facility (NEIF) Radiocarbon Laboratory, SUERC, UK, Radiocarbon, <https://doi.org/10.1017/RDC.2024.9>, 2024.
- Azpiroz-Zabala, M., Cartigny, M. J. B., Talling, P. J., Parsons, D. R., Sumner, E. J., Clare, M. A., Simmons, S. M., Cooper, C., and Pope, E. L.: Newly recognized turbidity current structure can explain prolonged flushing of submarine canyons, *Science Advances*, 3, e1700200, <https://doi.org/10.1126/sciadv.1700200>, 2017.
- Babonneau, N., Savoye, B., Cremer, M., and Klein, B.: Morphology and Architecture of the present canyon and channel system of the Zaire deep-sea fan, *Mar. Petrol. Geol.*, 19, 445–467, 2002.
- Babonneau, N., Savoye, B., Cremer, M., and Bez, M.: Sedimentary Architecture in Meanders of a Submarine Channel: Detailed Study of the Present Congo Turbidite Channel (Zaiango Project), *J. Sediment. Res.*, 80, 852–866, <https://doi.org/10.2110/jsr.2010.078>, 2010.
- Baker, M. L., Hage, S., Talling, P. J., Acikalin, S., Hilton, R., Sahin, S., Ruffell, S. C., Pope, E. L., Silva Jacinto, R., and Clare, M. A.: Terrestrial organic carbon temporarily stored in submarine Congo Canyon is efficiently remobilised by canyon-flushing turbidity currents, *Geology*, 52, 631–636, 2024.
- Baudin, F., Disnar, J. R., Martinez, P., and Dennielou, B.: Distribution of the organic matter in the channel-levees systems of the Congo mud-rich deep sea fan (West Africa). Implication for deep offshore petroleum source rocks and global carbon cycle, *Mar. Petrol. Geol.*, 27, 995–1010, <https://doi.org/10.1016/j.marpetgeo.2010.02.006>, 2010.
- Baudin, F., Disnar, J. R., Aboussou, A., and Savignac, F.: Guidelines for Rock-Eval analysis of recent marine sediments, *Org. Geochem.*, 86, 71–80, <https://doi.org/10.1016/j.orggeochem.2015.06.009>, 2015.
- Baudin, F., Stetten, E., Schnyder, J., Charlier, K., Martinez, P., Dennielou, B., and Droz, L.: Origin and distribution of the organic matter in the distal lobe of the Congo deep-sea fan – A Rock-Eval survey, *Deep-Sea Res. Pt. II*, 142, 75–90, <https://doi.org/10.1016/j.dsr2.2017.01.008>, 2017.
- Baudin, F., Rabouille, C., and Dennielou, B.: Routing of terrestrial organic matter from the Congo River to the ultimate sink in the abyss: a mass balance approach, *Geol. Belg.*, 23, <https://doi.org/10.20341/gb.2020.004>, 2020.

- Berner, R. A.: Burial of organic carbon and pyrite sulfur in the modern ocean; its geochemical and environmental significance, *Am. J. Sci.*, 282, 451–473, 1982.
- Bouma, A. H.: *Sedimentology of Some Flysch Deposits*, Elsevier, Amsterdam, 1962.
- Brun, L., Pairaud, I., Jacinto, R. S., Garreau, P., and Dennielou, B.: Strong hydrodynamic processes observed in the Mediterranean Cassidaigne submarine canyon, *Front. Mar. Sci.*, 10, 1078831, <https://doi.org/10.3389/fmars.2023.1078831>, 2023.
- Burdige, D. J.: Preservation of organic matter in marine sediments: controls, mechanisms, and an imbalance in sediment organic carbon budgets?, *Chem. Rev.*, 107, 467–485, <https://doi.org/10.1021/cr050347q>, 2007.
- Canals, M., Puig, P., de Madron, X., Heussner, S., Palanques, A., and Fabres, J.: Flushing submarine canyons, *Nature*, 444, 354–357, <https://doi.org/10.1038/nature05271>, 2006.
- Cartigny, M. J. B., Ventra, D., Postma, G., van Den Berg, J. H., and Venditti, J.: “Morphodynamics and sedimentary structures of bedforms under supercritical-flow conditions: New insights from numerical experiments”, *Sedimentology*, 61, 712–748, 2014.
- Ciais, P., Sabine, C., Bala, G., Bopp, L., Brovkin, V., Canadell, J. G., Chhabra, A., DeFries, R., Galloway, J., Heimann, M., Jones, C., Le Quéré, C., Myneni, R., Piao, S., Thornton, P., Willem, J., Friedlingstein, P., and Munhoven, G.: Carbon and Other Biogeochemical Cycles, in: *Climate Change 2013: The Physical Science Basis, Contribution of Working Group I to the Fifth Assessment Report of the Intergovernmental Panel on Climate Change*, edited by: Intergovernmental Panel on Climate Change, Cambridge University Press, Cambridge, United Kingdom and New York, NY, USA, <https://doi.org/10.1017/CBO9781107415324.015>, 2013.
- Clare, M. A., Lintern, D. G., Rosenberger, K., Hughes Clarke, J. E., Paull, C. K., Gwiazda, R., Cartigny, M. J. B., Talling, P. J., Perara, D., Xu, J., Parsons, D. P., Silva Jacinto, R., and Apprioual, R.: Lessons learned from the monitoring of turbidity currents and guidance for future platform designs, *Geol. Soc. Spec. Publ.*, 500, 605–634, <https://doi.org/10.1144/SP500-2019-173>, 2020.
- Coyne, A., Seyler, P., Etcheber, H., Meybeck, M., and Orange, D.: Spatial and seasonal dynamics of total suspended sediment and organic carbon species in the Congo River, *Global Biogeochem. Cy.*, 19, 17, <https://doi.org/10.1029/2004GB002335>, 2005.
- Dennielou, B., Droz, L., Jacq, C., Babonneau, N., Bonnel, C., Picot, M., Le Saout, M., Saout, J., Bez, M., Savoye, B., Olu, K., and Rabouille, C.: Morphology, structure, composition and build-up processes of the active Congo channel-mouth lobe complex with inputs from remotely operated underwater vehicle (ROV) multibeam and video surveys, *Deep-Sea Res. Pt. II*, 142, 25–49, <https://doi.org/10.1016/j.dsr2.2017.03.010>, 2017.
- French, K. L., Hein, C. J., Haghipour, N., et al.: Millennial soil retention of terrestrial organic matter deposited in the Bengal Fan, *Sci. Rep.*, 8, 11997, <https://doi.org/10.1038/s41598-018-30091-8>, 2018.
- Friedlingstein, P., O’Sullivan, M., Jones, M. W., Andrew, R. M., Bakker, D. C. E., Hauck, J., Landschützer, P., Le Quéré, C., Luijkx, I. T., Peters, G. P., Peters, W., Pongratz, J., Schwingshackl, C., Sitch, S., Canadell, J. G., Ciais, P., Jackson, R. B., Alin, S. R., Anthoni, P., Barbero, L., Bates, N. R., Becker, M., Bellouin, N., Decharme, B., Bopp, L., Brasika, I. B. M., Cadule, P., Chamberlain, M. A., Chandra, N., Chau, T.-T.-T., Chevallier, F., Chini, L. P., Cronin, M., Dou, X., Enyo, K., Evans, W., Falk, S., Feely, R. A., Feng, L., Ford, D. J., Gasser, T., Ghattas, J., Gkritzalis, T., Grassi, G., Gregor, L., Gruber, N., Gürses, Ö., Harris, I., Hefner, M., Heinke, J., Houghton, R. A., Hurtt, G. C., Iida, Y., Ilyina, T., Jacobson, A. R., Jain, A., Jarníková, T., Jersild, A., Jiang, F., Jin, Z., Joos, F., Kato, E., Keeling, R. F., Kennedy, D., Klein Goldewijk, K., Knauer, J., Korsbakken, J. I., Körtzinger, A., Lan, X., Lefèvre, N., Li, H., Liu, J., Liu, Z., Ma, L., Marland, G., Mayot, N., McGuire, P. C., McKinley, G. A., Meyer, G., Morgan, E. J., Munro, D. R., Nakaoka, S.-I., Niwa, Y., O’Brien, K. M., Olsen, A., Omar, A. M., Ono, T., Paulsen, M., Pierrot, D., Pockock, K., Poulter, B., Powis, C. M., Rehder, G., Resplandy, L., Robertson, E., Rödenbeck, C., Rosan, T. M., Schwinger, J., Séférian, R., Smallman, T. L., Smith, S. M., Sospedra-Alfonso, R., Sun, Q., Sutton, A. J., Sweeney, C., Takao, S., Tans, P. P., Tian, H., Tilbrook, B., Tsujino, H., Tubiello, F., van der Werf, G. R., van Ooijen, E., Wanninkhof, R., Watanabe, M., Wimart-Rousseau, C., Yang, D., Yang, X., Yuan, W., Yue, X., Zaehle, S., Zeng, J., and Zheng, B.: *Global Carbon Budget 2023*, *Earth Syst. Sci. Data*, 15, 5301–5369, <https://doi.org/10.5194/essd-15-5301-2023>, 2023.
- Galy, V., France-Lanord, C., Beyssac, O., Faure, P., Kudrass, H., and Palhol, F.: Efficient organic carbon burial in the Bengal fan sustained by the Himalayan erosional system, *Nature*, 450, 407–410, 2007.
- Galy, V., Peucker-Ehrenbrink, B., and Eglinton, T.: Global carbon export from the terrestrial biosphere controlled by erosion, *Nature*, 521, 204–207, 2015.
- Gardner, W. D.: Field assessment of sediment traps, *J. Mar. Res.*, 38, 41–52, 1980.
- Garrett, C. and Kunze, E.: Internal tide generation in the deep ocean, *Annu. Rev. Fluid Mech.*, 39, 57–87, 2007.
- Ge, Z., Nemeč, W., Vellinga, A. J., and Gawthorpe, R. L.: How is a turbidite actually deposited?, *Sci. Adv.*, 8, eabl9124, <https://doi.org/10.1126/sciadv.abl9124>, 2022.
- Guiastrenec-Faugas, L., Gillet, H., Jacinto, R. S., Dennielou, B., Hanquiez, V., Schmidt, S., Simplet, L., and Rousset, A.: Upstream migrating knickpoints and related sedimentary processes in a submarine canyon from a rare 20 year morphobathymetric time-lapse (Capbreton submarine canyon, Bay of Biscay, France), *Mar. Geol.*, 423, 106143, <https://doi.org/10.1016/j.margeo.2020.106143>, 2020.
- Hage, S.: Particulate organic carbon measurements in the Congo Submarine Canyon, SEANOE [data set], <https://doi.org/10.17882/99616>, 2024.
- Hage, S., Galy, V. V., Cartigny, M. J. B., Acikalin, S., Clare, M. A., Gröcke, D. R., Hilton, R. G., Hunt, J. E., Lintern, D. G., McGhee, C. A., Parsons, D. R., Stacey, C. D., Sumner, E. J., and Talling, P. J.: Efficient preservation of young terrestrial organic carbon in sandy turbidity-current deposits, *Geology*, 48, 882–887, <https://doi.org/10.1130/G47320.1>, 2020.
- Harris, P. T. and Whiteway, T.: Global distribution of large submarine canyons: Geomorphic differences between active and passive continental margins, *Mar. Geol.*, 285, 69–86, <https://doi.org/10.1016/j.margeo.2011.05.008>, 2011.
- Hecky, R. E. and Hesslein, R. H.: Contributions of benthic algae to lake food webs as revealed by stable isotope analysis, *J. N. Am. Benthol. Soc.*, 14, 631–653, 1995.

- Heezen, B. C. and Ewing, W. M.: Turbidity currents and submarine slumps, and the 1929 Grand Banks [Newfoundland] earthquake, *Am. J. Sci.*, 250, 849–873, 1952.
- Heezen, B. C., Menzies, R. J., Schneider, E. D., Ewing, W. M., and Granelli, N. C. L.: Congo Submarine Canyon, *Am. Assoc. Petr. Geol. B.*, 48, 1126–1149, <https://doi.org/10.1306/BC743D7F-16BE-11D7-8645000102C1865D>, 1964.
- Heijnen, M. S., Mienis, F., Gates, A. R., Bett, B. J., Hall, R. A., Hunt, Kane, I. A., Pebody, C., Huevenne, V. A. I., Soutter, E. L., and Clare, M. A.: Challenging the highstand-dormant paradigm for land-detached submarine canyons, *Nat. Commun.*, 13, 3448, <https://doi.org/10.1038/s41467-022-31114-9>, 2022.
- Hemingway, J., Rothman, D., Grant, K., Rosengard, S., Eglinton, T., Derry, L., and Galy, V.: Mineral protection regulates long-term global preservation of natural organic carbon, *Nature*, 228–231, 570, <https://doi.org/10.1038/s41586-019-1280-6>, 2019.
- Hemingway, J. D., Schefuss, E., Spencer, R. G. M., Jean Dinga, B., Eglinton, T. I., McIntyre, C., and Galy, V. V.: Hydrologic controls on seasonal and inter-annual variability of Congo River particulate organic matter source and reservoir age, *Chem. Geol.*, 466, 454–465, <https://doi.org/10.1016/j.chemgeo.2017.06.034>, 2017.
- Hilton, R. G., Galy, A., Hovius, N., Kao, S. J., Horng, M. J., and Chen, H.: Climatic and geomorphic controls on the erosion of terrestrial biomass from subtropical mountain forest, *Global Biogeochem. Cy.*, 26, GB3014, <https://doi.org/10.1029/2012GB004314>, 2012.
- Hua, Q., Turnbull, J. C., Santos, G. M., Rakowski, A. Z., An-capichún, S., De Pol-Holz, R., Hammer, S., Lehman, S. J., Levin, I., Miller, J. B., Palmer, J. G., and Turney, C. S. M.: Atmospheric Radiocarbon for the period 1950–2019, *Radiocarbon*, 64, 723–745, <https://doi.org/10.1017/RDC.2021.95>, 2022.
- Hughes Clarke, J. E.: First wide-angle view of channelized turbidity currents links migrating cyclic steps to flow characteristics, *Nat. Commun.*, 7, 11896, <https://doi.org/10.1038/ncomms11896>, 2016.
- Kao, S.-J., Hilton, R. G., Selvaraj, K., Dai, M., Zehetner, F., Huang, J.-C., Hsu, S.-C., Sparkes, R., Liu, J. T., Lee, T.-Y., Yang, J.-Y. T., Galy, A., Xu, X., and Hovius, N.: Preservation of terrestrial organic carbon in marine sediments offshore Taiwan: mountain building and atmospheric carbon dioxide sequestration, *Earth Surf. Dynam.*, 2, 127–139, <https://doi.org/10.5194/esurf-2-127-2014>, 2014.
- Khripounoff, A., Vangriesheim, A., Babonneau, N., Crassous, P., Dennielou, B., and Savoye, B.: Direct observation of intense turbidity current activity in the Zaire submarine valley at 4000 m water depth, *Mar. Geol.*, 193, 151–158, 2003.
- Khripounoff, A., Crassous, P., Lo Bue, N., Dennielou, B., and Silva Jacinto, R.: Different types of sediment gravity flows detected in the Var submarine canyon (northwestern Mediterranean Sea), *Prog. Oceanogr.*, 106, 138–153, 2012.
- Kneller, B. and Buckee, C.: The structure and fluid mechanics of turbidity currents: a review of some recent studies and their geological implications, *Sedimentology*, 47, 62–94, 2000.
- Lahaye, N., Gula, J., Thurnherr, A. M., Reverdin, G., Bouruet-Aubertot, P., and Roulet, G.: Deep currents in the rift valley of the north mid-Atlantic ridge, *Frontiers in Marine Science*, 6, 597, <https://doi.org/10.3389/fmars.2019.00597>, 2019.
- Laraque, A., Le Coz, J., Moukandi N’kaya, G. D., Bissemou, G., Ayissou, L., Rouché, N., Bricquet, J.-P., Yepez, S., and Gulemvuga, G.: Courbes de tarage du fleuve Congo à Brazzaville-Kinshasa, *LHB Hydroscience Journal*, 108, <https://doi.org/10.1080/27678490.2022.2082338>, 2022.
- Lee, H., Galy, V., Feng, X., Ponton, C., Galy, A., France-Lanord, C., and Feakins, S. J.: Sustained wood burial in the Bengal Fan over the last 19 My, *P. Natl. Acad. Sci. USA*, 116, 22518–22525, 2019.
- Li, M. Z., Prescott, R. H., and Robertson, A. G.: Observation of internal tides and sediment transport processes at the head of Logan Canyon on central Scotian Slope, eastern Canada, *J. Marine Syst.*, 193, 103–125, 2019.
- Liu, J. T., Hsu, R. T., Hung, J.-J., Chang, Y.-P., Wang, Y.-H., Rendle-Buhring, R. H., Lee, C.-L., Huh, C.-A., and Yang, R. J.: From the highest to the deepest: the Gaoping River – Gaoping Submarine Canyon dispersal system, *Earth Sci. Rev.*, 153, 274–300, <https://doi.org/10.1016/j.earscirev.2015.10.012>, 2016.
- Maier, K. L., Rosenberg, K. J., Paull, C. K., Gwiazda, R., Gales, J., Lorensen, T., Barry, J. P., Talling, P. J., McGann, M., Xu, J., Lundsten, E., Anderson, K., Litvin, S. Y., Parsons, D. R., Clare, M. A., Simmons, S. M., Sumner, E. J., and Cartigny, M. J. B.: Sediment and organic carbon transport and deposition driven by internal tides along Monterey Canyon, offshore California, *Deep-Sea Res. Pt. I*, 153, 103108, <https://doi.org/10.1016/j.dsr.2019.103108>, 2019.
- Mariotti, A., Gadel, F., Giresse, P., and Kinga-Mouzeo: Carbon Isotope compositions and geochemistry of particulate matter in the Congo River (Central Africa): Application to the study of Quaternary sediments off the mouth of the river, *Chem. Geol.*, 86, 345–357, 1991.
- Masson, D. G., Huvenne, V. A. I., de Stigter, H. D., Wolff, G. A., Kiriakoulakis, K., Arzola, R. G., and Blackbird, S.: Efficient burial of carbon in a submarine canyon, *Geology*, 38, 831–834, <https://doi.org/10.1130/G30895.1>, 2010.
- McArthur, A. D., Kneller, B. C., Wakefield, M. I., Souza, P. A., and Kuchle, J.: Palynofacies classification of the depositional elements of confined turbidite systems: Examples from the Gres d’Annot, SE France, *Mar. Petrol. Geol.*, 77, 1254–1273, 2016.
- Middelburg, J. J.: A simple rate model for organic-matter decomposition in marine-sediments, *Geochim. Cosmochim. Ac.*, 53, 1577–1581, 1989.
- Miramontes, E., Eggenhuisen, J. T., Silva Jacinto, R., Poneti, G., Pohl, F., Normandeau, A., Campbell, D. C., and Hernandez-Molina, J.: Channel-levee evolution in combined contour current–turbidity current flows from flume-tank experiments, *Geology*, 48, 353–357, <https://doi.org/10.1130/G471111.1>, 2020.
- Mollenhauer, G., Schneider, R. R., Jennerjahn, T., Muller, P. J., and Wefer, G.: Organic carbon accumulation in the South Atlantic Ocean: its modern, mid-Holocene and last glacial distribution, *Global Planet. Change*, 40, 249–266, 2004.
- Mook, W. G. and van der Plicht, J.: Reporting ¹⁴C activities and concentrations, *Radiocarbon*, 41, 227–239, 1999.
- Mulder, T., Zaragosi, S., Garlan, T., Mavel, J., Cremer, M., Sottolichio, A., Sénéchal, N., and Schmidt, S.: Present deep-submarine canyons activity in the Bay of Biscay (NE Atlantic), *Mar. Geol.*, 295–298, 113–127, 2012.
- Normandeau, A., Dafoe, L. T., Li, M. Z., Campbell, D. C., and Jenner, K. A.: Sedimentary record of bottom currents and internal

- tides in a modern highstand submarine canyon head, *Sedimentology*, 71, 1061–1083, <https://doi.org/10.1111/sed.13165>, 2024.
- Paull, C. K., Ussler III, W., Mitts, P. J., Caress, D. W., and West, G. J.: Discordant ^{14}C stratigraphies in upper Monterey Canyon: a signal of anthropogenic disturbance, *Mar. Geol.*, 233, 21–36, <https://doi.org/10.1016/j.margeo.2006.07.008>, 2006.
- Paull, C. K., Talling, P. J., Maier, K. L., Parsons, D. P., Xu, J., Caress, D. W., Gwiazda, R., Lundsten, E. V., Anderson, K., Barry, J. P., Chaffey, M., O'Reilly, T., Rosenberg, K. J., Gales, J. A., Kieft, B., McGann, M., Simmons, S. M., McCann, M., Sumner, E. J., Clare, M. A., and Cartigny, M. J. B.: Powerful turbidity currents driven by dense basal layers, *Nat. Commun.*, 9, 4114, <https://doi.org/10.1038/s41467-018-06254-6>, 2018.
- Pope, E. L., Heijnen, M. S., Talling, P. J., Silva Jacinto, R., Gailot, A., Baker, M. L., Hage, S., Hasenhündl, M., Heerema, C. J., McGhee, C., Ruffel, S. C., Simmons, S. M., Cartigny, M. J. B., Clare, M. A., Dennielou, B., Parsons, D. R., Peirce, C., and Urlaub, M.: Landslide-dams affect sediment and carbon fluxes in deep-sea submarine canyons, *Nat. Geosci.*, 13, 4193, <https://doi.org/10.1038/s41561-022-01017-x>, 2022.
- Posamentier, H. W. and Kolla, V.: Seismic geomorphology and stratigraphy of depositional elements in deep-water settings, *J. Sediment. Res.*, 73, 367–368, 2003.
- Prahl, F. G., de Lange, G. J., Scholten, S., and Cowie, G. L.: A case of post-depositional degradation of terrestrial organic matter in turbidite deposits from Madeira Abyssal Plain, *Org. Geochem.*, 27, 141–152, 1997.
- Puig, P., Palanques, A., and Martin, J.: Contemporary sediment-transport processes in submarine canyons, *Annu. Rev. Mar. Sci.*, 6, <https://doi.org/10.1146/annurev-marine-010213-135037>, 2014.
- Rabouille, C., Caprais, J. C., Lansard, B., Crassous, P., Dedieu, K., Reyss, J. L., and Khripounoff, A.: Organic matter budget in the Southeast Atlantic continental margin close to the Congo Canyon: In situ measurements of sediment oxygen consumption, *Deep-Sea Res. Pt. II*, 56, 2223–2238, <https://doi.org/10.1016/j.dsr2.2009.04.005>, 2009.
- Rabouille, C., Baudin, F., Dennielou, B., and Olu, K.: Organic carbon transfer and ecosystem functioning in the terminal lobes of the Congo deep-sea fan: outcomes of the Congolobe project, *Deep-Sea Res. Pt. II*, 142, 1–6, <https://doi.org/10.1016/j.dsr2.2017.07.006>, 2017a.
- Rabouille, C., Olu, K., Baudin, F., Khripounoff, A., Dennielou, B., Arnaud-Haond, S., Babonneau, N., Bayle, C., Beckler, J., Bessette, S., Bomble, B., Bourgeois, S., Brandily, C., Caprais, J. C., Cathalot, C., Charlier, K., Corvaisier, R., Croguennec, C., Cruaud, P., Decker, C., Droz, L., Gayet, N., Godfroy, A., Hourdez, S., Le Bruchec, J., Le Saout, J., Lesaout, M., Lesongeur, F., Martinez, P., Mejanelle, L., Michalopoulos, P., Mouchel, O., Noel, P., Pastor, L., Picot, M., Pignet, P., Pozzato, L., Pruski, A. M., Rabiller, M., Raimonet, M., Ragueneau, O., Reyss, J. L., Rodier, P., Ruesch, B., Ruffine, L., Savignac, F., Senyarrich, C., Schnyder, J., Sen, A., Stetten, E., Sun, M. Y., Taillefert, M., Teixeira, S., Tisnerat-Laborde, N., Toffin, L., Tourolle, J., Toussaint, F., Vétion, G., Jouanneau, J. M., and Bez, M.: The Congolobe project, a multidisciplinary study of Congo deep-sea fanlobe complex: Overview of methods, strategies, observations and sampling, *Deep-Sea Res. Pt. II*, 142, 7–24, <https://doi.org/10.1016/j.dsr2.2016.05.006>, 2017b.
- Rabouille, C., Dennielou, B., Baudin, F., Raimonet, M., Droz, L., Khripounoff, A., Martinez, P., Mejanelle, L., Michalopoulos, P., Pastor, L., Pruski, A., Ragueneau, O., Reyss, J.-L., Ruffine, L., Schnyder, J., Stetten, E., Taillefert, M., Tourolle, J., and Olu, K.: Carbon and silica megasink in deep-sea sediments of the Congo terminal lobes, *Quaternary Sci. Rev.*, 222, 105854, <https://doi.org/10.1016/j.quascirev.2019.07.036>, 2019.
- Regnier, P., Friedlingstein, P., Ciais, P., Mackenzie, F. T., Gruber, N., Janssens, I. A., Laruelle, G. G., Lauerwald, R., Luyssaert, S., Andersson, A. J., Arndt, S., Arnosti, C., Borges, A. V., Dale, A. W., Gallego-Sala, A., Goddérís, Y., Goossens, N., Hartmann, J., Heinze, C., Ilyina, T., Joos, F., LaRowe, D. E., Leifeld, J., Meysman, F. J. R., Munhoven, G., Raymond, P. A., Spahni, R., Suntharalingam, P., and Thullner, M.: Anthropogenic perturbation of the carbon fluxes from land to ocean, *Nat. Geosci.*, 6, 597–607, 2013.
- Regnier, P., Resplandy, L., Najjar, R. G., and Ciais, P.: The land-to-ocean loops of the global carbon cycle, *Nature*, 603, 401–410, <https://doi.org/10.1038/s41586-021-04339-9>, 2022.
- Reimer, P. J., Brown, T. A., and Reimer, R. W.: Discussion: reporting and calibration of post-bomb ^{14}C data, *Radiocarbon*, 46, 1299–1304, 2004.
- Saller, A., Lin, R., and Dunham, J.: Leaves in turbidite sands: The main source of oil and gas in the deep-water Kutei Basin, Indonesia, *Am. Assoc. Petr. Geol. B.*, 90, 1585–1608, <https://doi.org/10.1306/04110605127>, 2006.
- Savoye, B., Cochonat, P., Apprioual, R., Bain, O., Baltzer, A., Bellec, V., Beuzart, P., Bourillet, J., Cagna, R., Cremer, M., Crusson, A., Dennielou, B., Diebler, D., Droz, L., Ennes, J., Floch, G., Foucher, J., Guiomar, M., Harmegnies, F., Kerbrat, R., Klein, B., Khun, H., Landure, J., Lasnier, C., Le Drezen, E., Le Formal, J., Lopez, M., Loubrieu, B., Marsset, T., Migeon, S., Normand, A., Nouze, H., Ondreas, H., Pelleau, P., Saget, P., Seranne, M., Sibuet, J. C., Tofani, R., and Voisset, M.: Structure et évolution récente de l'éventail turbiditique du Zaïre: Premiers résultats scientifiques des missions d'exploration ZaïAngo 1 and 2 (marge Congo-Angola), *C.R. Acad. Sci. II A*, 311, 211–220, [https://doi.org/10.1016/S1251-8050\(00\)01385-9](https://doi.org/10.1016/S1251-8050(00)01385-9), 2000.
- Sequeiros, O. E., Naruse, H., Endo, N., Garcia, M. H., and Parker, G.: Experimental study on self-accelerating turbidity currents, *J. Geophys. Res.*, 114, C05025, <https://doi.org/10.1029/2008JC005149>, 2009.
- Simmons, S. M., Azpiroz-Zabala, M., Cartigny, M. J. B., Clare, M. A., Cooper, C., Parsons, D. R., Pope, E. L., Sumner, E. J., and Talling, P. J.: Novel acoustic method provides first detailed measurements of sediment concentration structure within submarine turbidity currents, *J. Geophys. Res.-Oceans*, 125, e2019JC015904, <https://doi.org/10.1029/2019JC015904>, 2020.
- Skinner, L. C. and Bard, E.: Radiocarbon as a dating tool and tracer in paleoceanography, *Rev. Geophys.*, 60, e2020RG000720, <https://doi.org/10.1029/2020RG000720>, 2022.
- Soulet, G., Skinner, L. C., Beaupré, S. R., and Galy, V.: A note on reporting of reservoir ^{14}C disequilibria and age offsets, *Radiocarbon*, 58, 205–221, 2016.
- Spencer, R. G. M., Hernes, P. J., Aufdenkampe, A. K., Baker, A., Gulliver, P., Stubbins, A., Aiken, G. R., Dyda, R. Y., Butler, K. D., Mwamba, V. L., Mangangu, A. M., Wabakghanzi, J. N., and Six, J.: An initial investigation into the organic matter bio-

- geochemistry of the Congo River, *Geochim. Cosmochim. Ac.*, 84, 614–627, <https://doi.org/10.1016/j.gca.2012.01.013>, 2012.
- Stetten, E., Baudin, F., Reyss, J. L., Martinez, P., Charlier, K., Schnyder, J., Rabouille, C., Dennielou, B., Coston-Guarini, J., and Pruski, A.: Organic matter characterization and distribution in sediments of the terminal lobes of the Congo deep-sea fan: evidence for the direct influence of the Congo River, *Mar. Geol.*, 369, 182–195, <https://doi.org/10.1016/j.margeo.2015.08.020>, 2015.
- Stuiver, M. and Polach, H. A.: Discussion: reporting of ^{14}C data, *Radiocarbon*, 19, 355–363, 1977.
- Sumner, E. J. and Paull, C. K.: Swept away by a turbidity current in Mendocino submarine canyon, California, *Geophys. Res. Lett.*, 41, 7611–7618, <https://doi.org/10.1002/2014GL061863>, 2014.
- Symons, W. O., Sumner, E. J., Paull, C. K., Cartigny, M. J. B., Xu, J. P., Maier, K. L., Lorenson, T. D., and Talling, P. J.: A new model for turbidity current behavior based on integration of flow monitoring and precision coring in a submarine canyon, *Geology*, 45, 367–370, <https://doi.org/10.1130/G38764.1>, 2017.
- Talling, P. J., Baker, M. L., Pope, E. L., Ruffell, S. C., Silva Jacinto, R., Heijnen, M. S., Hage, S., Simmons, S. M., Hasenhündl, M., Heerema, C. J., McGhee, C., Apprioual, R., Ferrant, A., Cartigny, M. J. B., Parsons, D. R., Clare, M. A., Tshimanga, R. M., Trigg, M. A., Cula, C. A., Faria, C. A., Gaillet, A., Bola, G., Wallace, D., Griffiths, A., Nunny, R., Urlaub, M., Peirce, C., Burnett, R., Neasham, J., and Hilton, R. J.: Longest sediment flows yet measured show how major rivers connect efficiently to deep sea, *Nat. Commun.*, 13, 4193, <https://doi.org/10.1038/s41467-022-31689-3>, 2022.
- Talling, P. J., Cartigny, M. J. B., Pope, E., Baker, M., Clare, M. A., Heijnen, M., Hage, S., Parsons, D. R., Simmons, S. M., Paull, C. K., Gwiazda, R., Lintern, G., Hughes Clarke, J. E., Xu, J., Silva Jacinto, R., and Maier, K. L.: Detailed monitoring reveals the nature of submarine turbidity currents, *Nature Reviews Earth & Environment*, 4, 642–658, <https://doi.org/10.1038/s43017-023-00458-1>, 2023.
- Talling, P. J., Hage, S., Baker, M., Hilton, R., Bianchi, D., and Maier, K.: The global turbidity current pump and its implications for organic carbon cycling, *Annu. Rev. Mar. Sci.*, 16, 105–133, <https://doi.org/10.1146/annurev-marine-032223-103626>, 2024.
- Tegler, L. A., Horner, T. J., Galy, V., Bent, S. M., Wang, Y., Kim, H. H., Mete, O. Z., and Nielsen, S. G.: Distribution and drivers of organic carbon sedimentation along the continental margins, *AGU Adv.* 5, e2023AV001000, <https://doi.org/10.1029/2023AV001000>, 2024.
- Treignier, C., Derenne, S., and Saliot, A.: Terrestrial and marine n-alcohol inputs and degradation processes relating to a sudden turbidity current in the Zaire canyon, *Org. Geochem.*, 37, 1170–1184, <https://doi.org/10.1016/j.orggeochem.2006.03.010>, 2006.
- Vallaëys, V., Lambrechts, J., Delandmeter, P., Pättsch, J., Spitz, A., Hanert, E., and Deleersnijder, E.: Understanding the circulation in the deep, micro-tidal and strongly stratified Congo River estuary, *Ocean Model.*, 167, 101890, <https://doi.org/10.1016/j.ocemod.2021.101890>, 2021.
- van der Voort, T. S., Blattmann, T. M., Usman, M., Montluçon, D., Loeffler, T., Tavagna, M. L., Gruber, N., and Eglinton, T. I.: MOSAIC (Modern Ocean Sediment Archive and Inventory of Carbon): a (radio)carbon-centric database for seafloor surficial sediments, *Earth Syst. Sci. Data*, 13, 2135–2146, <https://doi.org/10.5194/essd-13-2135-2021>, 2021.
- Vangriesheim, A., Khripounoff, A., and Crassous, P.: Turbidity events observed in situ along the Congo submarine channel, *Deep-Sea Res. Pt. II*, 56, 2208–2222, <https://doi.org/10.1016/j.dsr2.2009.04.004>, 2009.
- Welch, P.: The use of the fast Fourier transform for the estimation of power spectra: A method based on time averaging over short, modified periodograms, *IEEE T. Acoust. Speech.*, 15, 70–73, 1967.